5. Ultraviolet photoelectron spectroscopy from CaF_2

5.1 Introduction

Ultraviolet photoelectron spectroscopy is a standard method for the investigation of electronic states in metals and semiconductors. For insulating crystals, comparatively few UPS investigations were reported in literature. One reason for this fact might be that in the past insulators in general have attracted less interest than other materials. However, there is also the severe experimental problem of sample charging and radiation damage making experiments with bulk crystals difficult or impossible to perform. During the last ten years, a number of reports on photoemission from CaF_2 thin films evaporated on a variety of semiconductors were published in literature. These investigations were concerned with the epitaxial growth conditions of fluorites on semiconductors [OBr90a], [DRH95], [HLO95], band alignment [CTR91] and the electronic structure at the interface [HHM89], [DMK97]. In contrast to previous work, the present investigation is focussed on both, bulk crystals and thin films, and important information was obtained from a comparison of the results from both samples.

In this thesis, first UPS measurements performed on CaF_2 bulk crystals cleaved in UHV are presented. The crystals were heated to avoid strong charging. The conduction mechanism activated by heating is investigated and all experimental findings with regard to sample charging can consistently be explained by a model proposing V_K-center diffusion. The influence of electron-phonon interaction on the photoelectron angular distribution in photoemission is demonstrated.

Fluoride materials are commonly believed to be rather stable and chemically inert. In the present thesis, however, it is shown that the surface stoichiometry of the crystal can strongly be changed by exposure to air, and such contamination cannot simply be removed by heating. It was found that the predominant impurity is oxygen. Oxygen adsorption was investigated on both, bulk samples and epitaxial thin films.

Changes of the electronic structure of CaF_2 were induced by 1.5 to 2.5 keV electron irradiation and 21.2 eV photon irradiation. Metallization and beam induced reactions with oxygen were investigated.

5.2. Basic features

5.2.1 Introduction

This chapter covers phenomena that are specific to photoemission from CaF_2 as an ionic material. The energy distribution curve of CaF_2 is presented and spectral features are compared to predictions of a band structure calculation [HLi80] and the Born model binding energy [PSL75]. Then, the importance of electron-phonon interaction in insulator photoemission is investigated. This subject was studied earlier by Himpsel and Steinmann [HSt75] for NaCl with synchrotron radiation. At excitation energies below the electron-electron scattering threshold, that the angular distribution of photoelectrons was observed to depend on the final state band only. This effect was attributed to electron-phonon scattering. In the present thesis, similar observations were made in photoemission from films of different thickness. Further, phonon excitation during photoemission from localized states also accounts for a large part of the observed width of the peaks, as was shown by Citrin et al [CEH74] for a number of alkali halides. Here, this effect could be demonstrated for valence band photoemission from CaF_2. The last part of this section deals with the electric conductivity of CaF_2. To activate conductivity in order to reduce charging under photon irradiation, it was necessary to heat the crystals. The microscopic nature of the thermally activated conduction mechanism is analyzed, and a model is proposed that accounts for all observations related to surface charging under UV irradiation.

5.2.2 Photoemission from the UHV cleaved surface and energy reference

In this section, a typical photoemission spectrum from a calcium fluoride single crystal is presented and the observed features are compared to the results of a band structure calculation. The problem of finding a reliable energy reference point in the spectrum that can be used to establish a binding energy scale is discussed. It will be shown that no such point, like the Fermi step for metals, exists in CaF_2. Therefore, in all spectra presented here, the photoelectron yield is shown as a function of the electron kinetic energy instead of the binding energy.

A normal emission ultraviolet photoelectron spectrum of a CaF_2 (111) single crystal surface prepared by cleavage in UHV is shown in Fig. 5.1. To reduce charging, the crystal was heated to 530 K during the measurement.

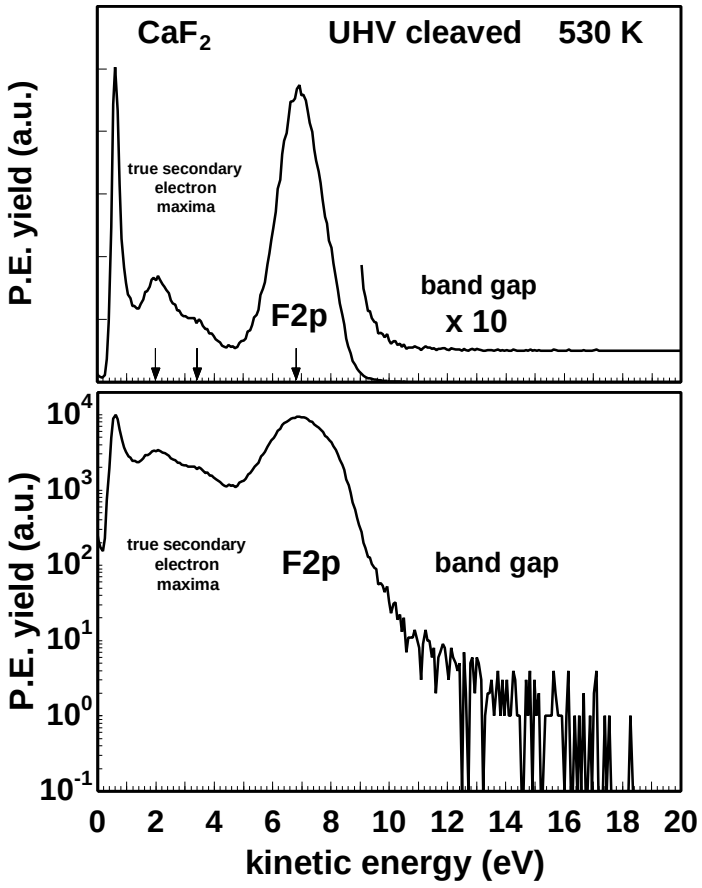

Fig 5.1 Linear and logarithmic plot of the normal emission energy distribution curve (EDC) from a CaF_2 crystal that was cleaved in UHV. The crystal was heated to 530 K to reduce charging. A bias of -2 V was applied to prevent the low energy secondary electrons from being retracted on the sample. In this figure, the position of the valence band peak maximum is at 6.8 eV kinetic energy (see arrow), the positions of the two secondary electron maxima are at 3.4 and 2.0 eV kinetic energy, respectively.

Several structures are visible in the spectrum. The most prominent feature is the F2p valence band peak extending from 5 to 9 eV kinetic energy with a maximum at 6.8 eV. At the low kinetic energy side of the valence band peak, a monotonously decreasing background is observed that is superimposed by two true secondary electron maxima at 3.4 and 4.8 eV below the valence band maximum. At very low kinetic energy (< 1 eV), unspecific secondary emission with a high yield is found. There is no clear step separating the valence band emission from the bandgap in the spectrum. Instead, a rapidly decreasing tail of electronic states extending several eV into the bandgap is observed. Possible sources of this emission are phonon broadening as discussed below, and electronic states related to structural imperfections in the bulk and at the stepped surface [PPH98] or impurities incorporated into the crystal during growth. Part of this emission above 9 eV kinetic energy may also be due to the satellite lines of the HeI 21.2 eV main line, at 23.09, 23.75, and 24.05 eV (compare to Fig. 4.3).

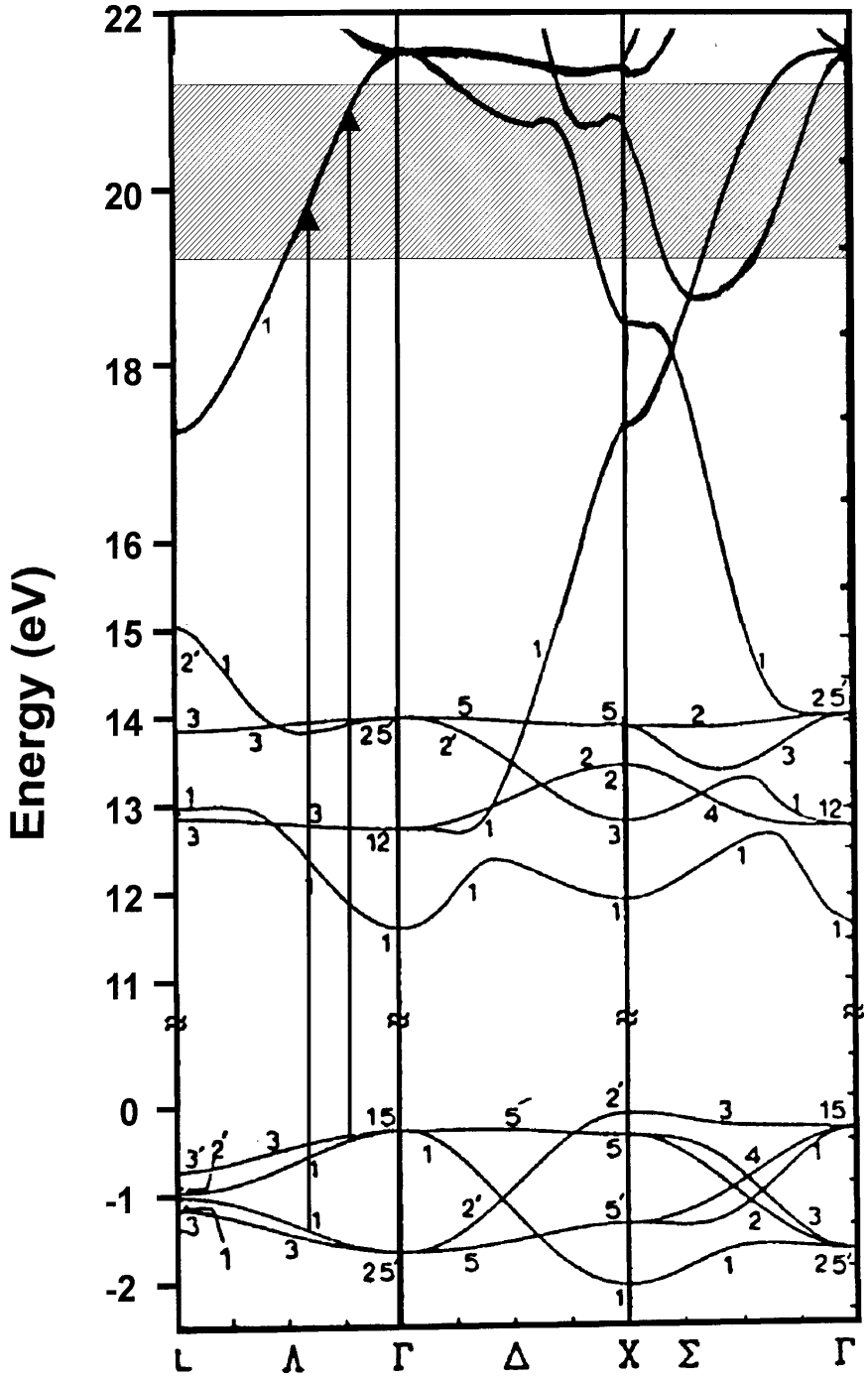

Fig. 5.2. Bandstructure of CaF_2 [HLi80]. For the use in the present work, the calculated band gap of 9.8 eV [HLi80] was expanded to reach the experimentally determined value of 11.6 eV [BJC90]. The shaded area marks the energy interval into which valence band electrons can be excited by HeI radiation. The two arrows symbolize photoexcitation with 21.2 eV in the Λ-direction which is the normal emission direction when investigating a (111)-plane. The valence band width in this calculation was 2 eV, which seems to be rather small compared with experimental results, also in [GXH92], a width of 3.1 eV was calculated.

The features observed in the spectrum can be assigned to energy bands in the CaF_2 band structure shown in Fig. 5.2. The band structure was taken from the work of Heaton and Lin [HLi80]; for the use in this thesis, the calculated band gap of 9.8 eV was corrected by adding 1.8 eV to reach the experimentally determined value of 11.6 eV [BJC90]. However, it has to be kept in mind that only qualitative agreement between theory and experiment can be expected, since there are uncertainties of the band positions in different bandstructure calculations published in literature [AJG77], [HLi80], [GXH92]. Final state bands that can be excited from the valence band by 21.2 eV irradiation are indicated by the hatched area in Fig. 5.2. Normal emission from the (111) plane corresponds to the ΓΛL line in the k-vector space (compare to the fcc Brillouin zone shown in Fig. 3.5). The valence band peak corresponds to electrons photo-excited into the topmost Λ_1 conduction band that is depicted in Fig. 5.2. The two true secondary electron maxima are caused by electrons that are emitted from the lower

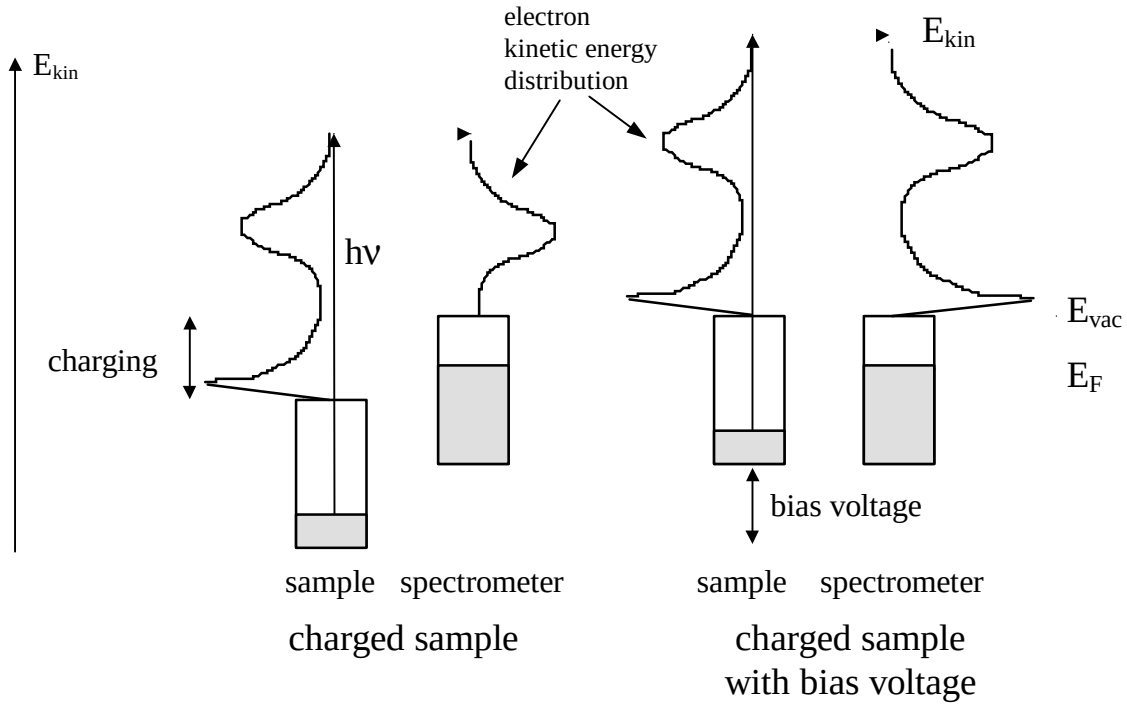

Fig. 5.3 Schematic energy diagram explaining the bias voltage method that is used to compensate sample charging to ensure the detection of the complete secondary electron distribution. Low energy secondary electrons photoemitted from a charged sample do not reach the detector, since they are retracted by the positive surface potential. Only the high energy part of the spectrum is detected (left hand side of the figure). To compensate for charging, a bias voltage is applied to the sample. It is increased until the vacuum level of sample and spectrometer coincide. Now, all secondary electrons are collected (right hand side of the figure).

lying conduction bands at about 14 eV (Λ_1 band from $\Gamma_{25'}$ to $L_{2'}$ in Fig. 5.2) and 12.9 eV (Λ_1 band from Γ_1 to L_1 in Fig. 5.2). These bands are populated by photoexcited electrons from the bands contained in hatched region that have lost energy in scattering events. The Λ_3 bands are not expected to contribute to the observed secondary electron emission as they have no amplitude in normal emission direction [EHi80] (see Chapter 3).

The position of the vacuum level relative to the other spectral features was determined using the negative bias voltage method [HRM97]. For a positive charged sample, the position of the sample vacuum level is below the vacuum level of the spectrometer. In this situation, the low energy part of the secondary electron tail does not reach the spectrometer and is not detected, as is schematically depicted in Fig. 5.3.

To overcome this problem, in addition to heating, a small bias voltage is applied to the sample to ensure the collection of all electrons from the secondary electron tail. The bias voltage is

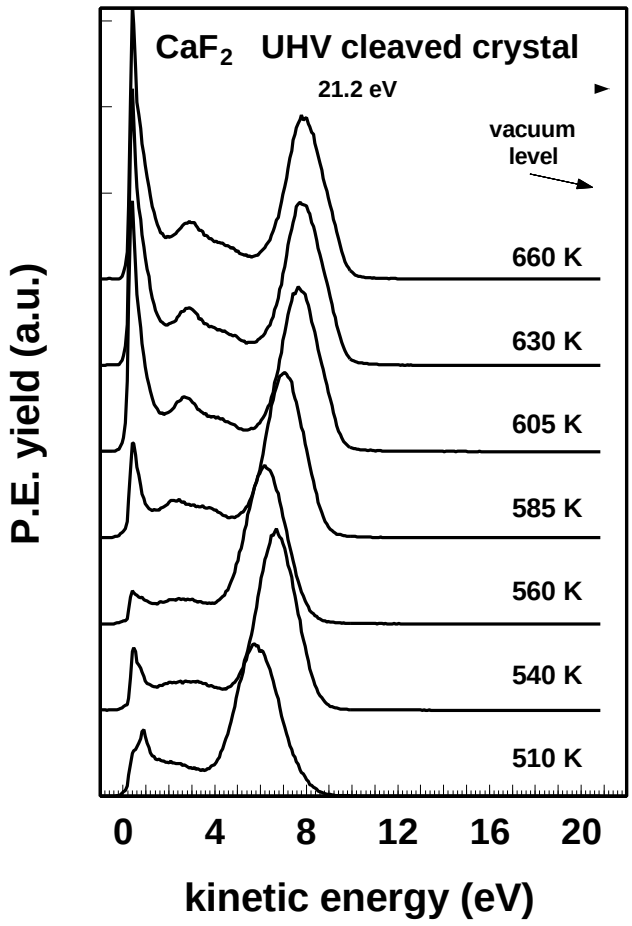

Fig 5.4 Normal emission spectra from a UHV cleaved CaF_2 crystal heated to different temperatures. A bias voltage of -1 V (bottom two spectra: -2 V) was applied to prevent the low energy secondary electrons from being retracted on the sample. The secondary electron tails were shifted to the same energy.

increased until the vacuum potential of the sample is at the same level as the vacuum potential of the spectrometer. When this condition is reached, the entire secondary electron tail appears in the spectrum. The position of the sample vacuum potential is then obtained by adding the photon energy to that of the low energy cutoff. Spectra taken in this way from a biased CaF_2 crystal at different temperatures are shown in Fig. 5.4.

It can be seen that the position of the valence band peak relative to the vacuum level shifts as a function of temperature. The top three spectra in Fig. 5.4 that were recorded at the highest temperatures are almost at the same energetic position, which means that charging was fully compensated. It was found impossible to detect all secondary electrons from a sample at insufficiently high temperature, regardless of the applied bias voltage. Increasing the bias for example for the spectrum taken at 510 K would not reveal a larger part of the secondary electron tail, but shift the spectrum as it is to higher kinetic energy.

For the purpose of binding energy reference, the valence band peak position measured at a temperature of 660 K will be used. The position of the secondary electron maxima, which can directly be compared to the conduction bands in Fig. 5.2, is at 3.0 eV (Γ_1 - L_1) and 4.4 eV ($\Gamma_{25'}$ - $L_{2'}$) above the vacuum level. Subtracting the kinetic energy $E_{kin}(T)$ of 7.8 eV at that temperature from the vacuum level position which is at 21.2 eV in Fig. 5.4, a binding energy of the valence band peak maximum of -13.4 eV results. Thus, the measured value for the energy difference between the valence band peak maximum and the true secondary electron maximum originating from the lowest Λ_1 conduction band (Γ_1 - L_1) is 16.4 eV, compared to a difference of 14 eV that is predicted by the band structure calculation (see Fig. 5.5 for a compilation of the energy levels). The reason for this deviations is that the calculated band structure is not appropriate for a description of the photoexcitation process in a localized system like the valence band of CaF_2, as it does not include final state effects. The calculated valence band position in Fig. 5.2 corresponds to the n-electron ground state of the crystal. However, the final state that is produced by photoemission is lacking one electron compared to the ground state. The relation between the two states is not trivial, except in the case of wide valence band solids like for example copper where the photohole is immediately delocalized over the whole crystal and therefore final and ground state energies are almost identical.

The conduction bands in Fig. 5.2, however, represent states corresponding to an additional electron in the crystal, which means that the true secondary electron structures are well described by the bands shown in Fig. 5.2, since these states were not directly populated by

photoemission, but by inelastically scattered secondary electrons from higher lying conduction bands.

A theoretical description of binding energies that is better suited for localized systems is provided by the Born model [PSL75]. In first order approximation, the binding energy of a F2p-valence band electron in CaF_2 is obtained by adding the Madelung energy E_M to the binding energy E_{ion} of an electron in the outermost level of the free fluorine ion:

$$E_{F2p} = E_{ion} + E_M \qquad 5.1$$

Using data published in literature (E_M = 10.74 eV for the fluorine ion in CaF_2, E_{ion} = 3.59 eV, both values from [Hay74]), an approximate binding energy of a F2p electron of -14.33 eV is obtained. Two corrections may be added to equation 5.1, the repulsive energy E_r which

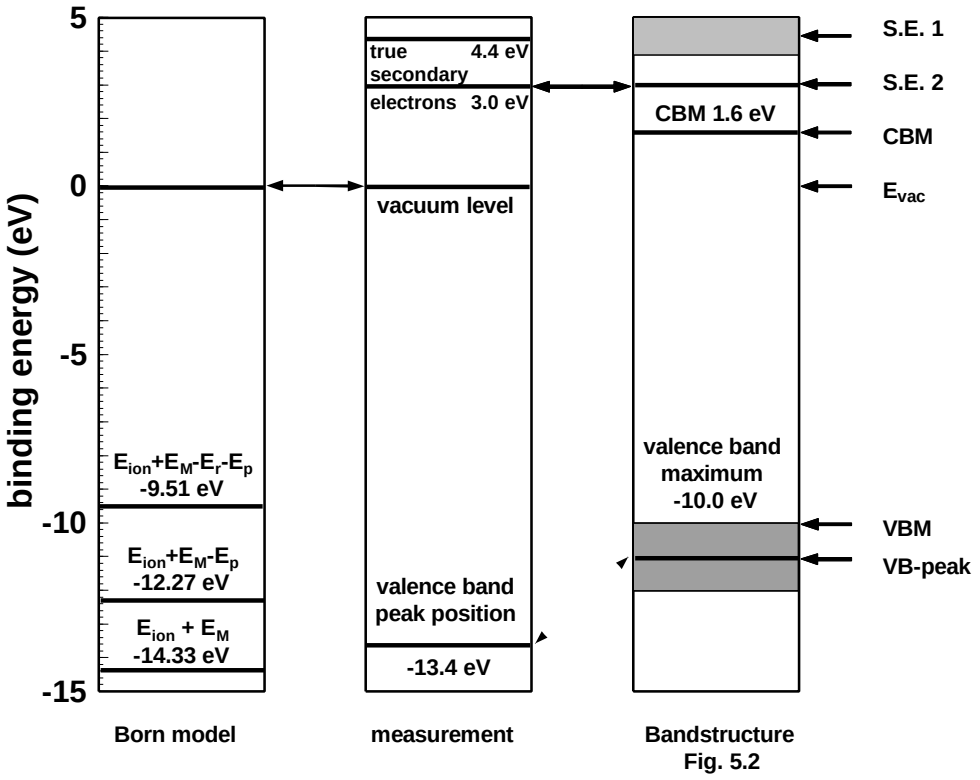

Fig 5.5 Energy level diagram summarizing Born model binding energies (left hand side of the figure), experimentally determined peak positions from Fig. 5.4 (middle), and the energy levels of the band structure calculation shown in Fig. 5.2 (right hand side of the figure). All energies are given with respect to the vacuum level. The bold double ended arrows indicate the levels in the different energy scales that were used for relative alignment. The valence band peak position in the middle energy scales (measurement) is assumed to correspond to the center of the valence band in the bandstructure picture (the level marked VB-peak). These two levels are connected by the dashed arrow.

accounts for the fact that the ion repels its neighbors in the initial state, thus lowering the energy, and the polarization energy E_p, which accounts for the final state effect of electronic polarization induced by the positive valence band hole that is produced in photoemission.

$$E_{F2p} = E_{ion} + E_M - E_r - E_p \qquad 5.2$$

For CaF_2, the repulsive energy E_r was calculated by Poole et al [PSL75] using the Born-Mayer repulsive potential. A value for E_r of 2.76 eV was determined. In the same work, a value for the polarization energy of 2.06 eV was given. A compilation of the various measured and calculated energy levels is shown in Fig. 5.5. The calculated Born-model theoretical value for the F2p binding energy is about 1 eV lower than the measured value as long as the Madelung energy alone is taken to represent the electron-crystal interaction, and 1.1 eV higher than the experimental value if additionally polarization effects are included into the calculation. Taking also the ion core repulsion energy into account results in a binding energy value that is much to high. A similar observation was made by Poole et al, who concluded that repulsive forces between the ions have negligible influence on the electronic levels [PSL75]. The valence band peak binding energy that was measured by Poole et al was at -12.3 eV, which gave excellent agreement with the Born model value including polarization energy. However, the spectra were obtained from thin films evaporated on aluminum, which is a less well defined sample than the crystals cleaved in UHV that were used in this work.

5.2.3 Phonon broadening of photoemission lines

Possible sources of broadening of insulator photoemission lines are inhomogeneous charging, limited lifetime of the photohole, and phonons. Phonon broadening has been found to be the dominant factor determining X-ray photoemission line width [CEH74]. This process is also effective in CaF_2, and, therefore, the width of the F2p peak cannot be directly compared to the calculated valence band width. For alkali halides, the experimentally determined contribution of phonons to the valence band width is between 0.6 and 1 eV at 500 K [WRB95]. In this section, temperature dependent broadening is investigated for CaF_2.

The origin of phonon broadening of photoemission lines can be understood within the Franck-Condon picture. The relaxation time of the nuclear motion is slow compared to the electronic excitation. Therefore, the excitation does not occur between the ground states of the initial and final state, but to a vibrationally excited level of the final electronic state (Fig. 5.6).

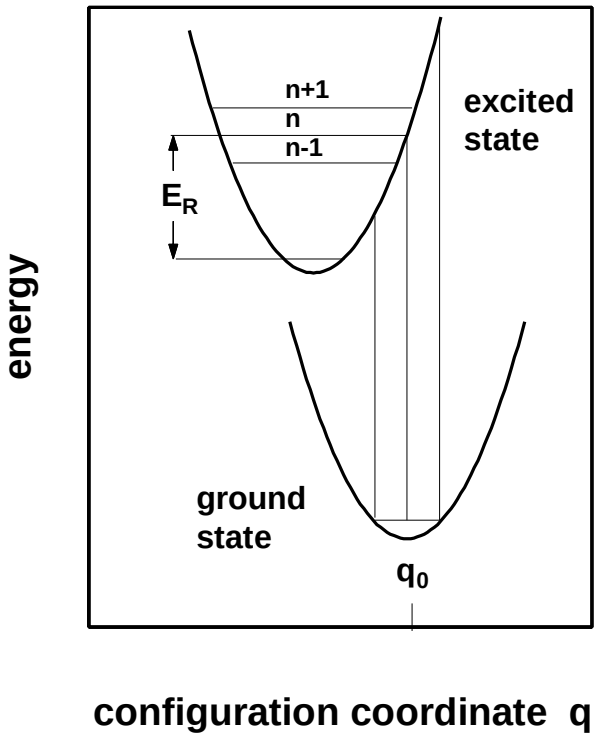

Fig 5.6 Simplified picture of the Franck-Condon principle giving schematically the energy of ground and excited state as a function of the configuration coordinate q, which is the distance between the nearest neighbor fluorine ions. The vibrational relaxation energy E_R is available for the excitation of phonons after photoionization.

In the Franck-Condon diagram, the vibrational relaxation energy E_R is the difference between the n-th vibrational state into which the photoexcitation is most likely to occur, and the bottom of the final state vibrational energy parabola. The lattice ground state zero point oscillation or motion at finite temperature is reflected in the width of the photoemission line, as various vibrational final states around the n-th state can be excited. This broadening process is not observed in conducting materials, where the photohole is immediately screened by the conduction band electrons from the rest of the lattice.

To investigate the contribution of phonon broadening to the valence band width of CaF_2, a number of normal emission spectra was taken in the temperature range from 490 K to 920 K. The valence band peak was fitted by a Gaussian function, and the respective widths are shown in Fig. 5.7. along with a theoretical curve that is discussed below.

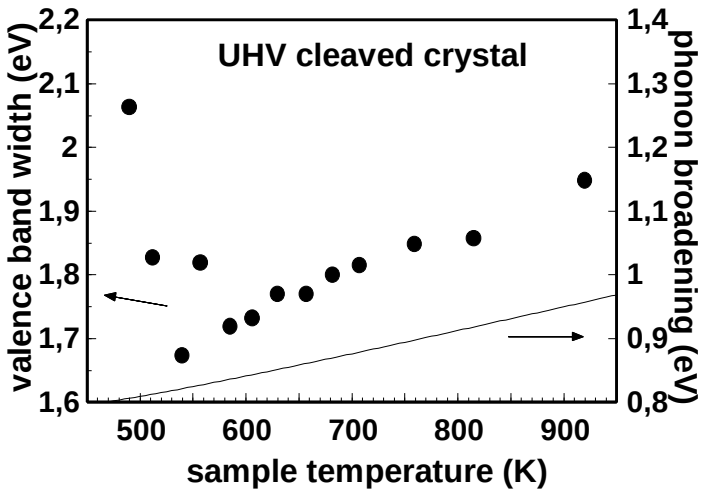

Fig 5.7 Valence band width of a CaF_2 crystals at different temperatures measured in normal emission. The valence band peak was fitted by a Gauss function, and the respective gaussian width is given in the figure (black dots). The solid line represents the calculated contribution of phonon broadening to the linewidth according to Eq. 5.4 [CEH74]. The crystal was cleaved in UHV

Below 600 K, inhomogenities in charging account for part of the valence band width. Note that the values in the negative sloped region of the curve correlate with the spectra in Fig. 5.4 with apparently higher binding energy. Peak broadening induced by charging decreases with increasing temperature due to thermally activated conductivity. The contribution of phonon broadening to the observed width increases with temperature.

The qualitative shape of the curve in Fig. 5.7 is similar to those observed by Citrin et al [CEH74] in their X-ray photoemission (XPS) investigation of core level linewidths of KF and KCl. In their work, an expression was derived for the XPS phonon linewidth that will be used here to estimate the valence band broadening. Using an expression that was derived for localized core holes is justified as valence band holes in ionic materials are well localized [Mah80]. A quantitative agreement between calculated and measured values cannot be expected since the valence band has a considerable intrinsic width opposite to core levels, however, information on the temperature dependence of phonon broadening can well be obtained.

The relaxation energy E_R was calculated by Citrin et al [CEH74] from the electron-LO phonon interaction Hamiltonian where the final state core hole is completely localized. The following simple formula is obtained:

$$E_R = \frac{e^2}{4pe_0}\left(\frac{6}{pV}\right)^{\frac{1}{3}}\left(\frac{1}{e_\infty}-\frac{1}{e_0}\right) \qquad 5.3$$

where ε_0 is the static and ε_∞ the dynamic dielectric constant. V is the volume of a primitive unit cell. Using data for CaF_2 (ε_0 = 6.81, ε_∞ = 2.04, V = 40.49 Å^3, all values from [Hay74]), a relaxation energy of 1.785 eV is calculated.

Provided a large number of phonons is excited (the average number of phonons is given by the Huang-Rhys factor $E_R / \hbar w_{LO}$, where ω_{LO} is the longitudinal optical phonon frequency at the Γ point), the lineshape is Gaussian and the linewidth (full width at half maximum) at a temperature T is given by [CEH74]:

$$\Delta E = 2.35 * \left(\hbar w_{LO} E_R \coth \frac{\hbar w_{LO}}{2kT} \right)^{\frac{1}{2}} \qquad 5.4$$

The solid line in Fig. 5.7 was drawn according to Eq 5.4 using a LO-phonon energy of 58 meV [Hay74]. The agreement between the slope of theoretical and experimental curves is not too favorable in the case of CaF_2 compared to alkali halides [CEH74], [IKu77].

The contribution of phonon broadening to the valence band linewidth is also a further reason why no clear valence band maximum can be found in the photoemission spectra, as the broadened top of the valence band has a Gaussian lineshape. Determining the valence band maximum would mean to qualify where the tail begins in the gaussian, which is ill defined.

5.2.4 Influence of electron-phonon interaction on photoelectron angular distribution

In the following part, the influence of electron-phonon interaction on angular resolved photoemission from CaF_2 is investigated. The photoelectron escape depth is found to be large compared to the electron-phonon scattering lengths, which means that in bulk materials or in thick films most photoemitted electrons experience several electron-phonon scattering events. The influence of scattering on the photoelectron angular distribution is demonstrated.

As a first step, the escape depth of photoelectrons in CaF_2 is determined. The photon energy used in this work (HeI, 21.2 eV) is below the electron-electron scattering threshold of CaF_2 which is equal to the sum of the bandgap and exciton energy [HSt78] (E_G+$E_{Exciton}$ = 11.6 eV + 11.2 eV = 22.8 eV for CaF_2). Electrons photoexcited by the HeI line are therefore not capable of loosing energy by scattering with valence band electrons. In this energy regime, the escape depth of photoelectrons from CaF_2 is much larger than indicated by the universal curve (Fig. 2.13). The escape depth λ_{el} of photoelectrons excited with hν = 21.2 eV from CaF_2 was determined from the dependence of the integrated F2p valence band photoemission yield from the thickness of the evaporated film (see Fig. 5.8).

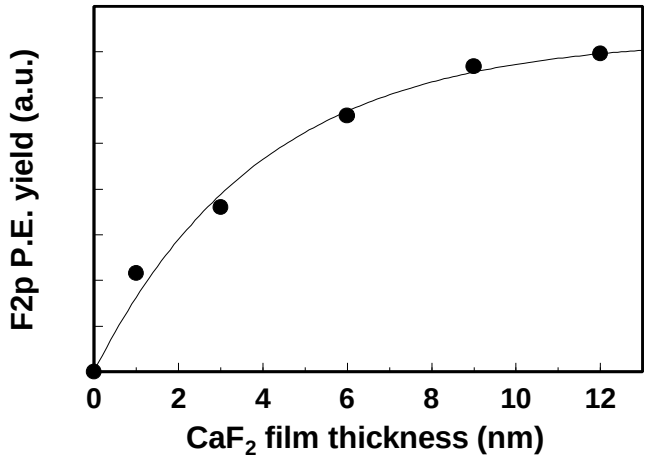

Fig. 5.8 Dependence of the integrated F2p valence band photoemission signal from film thickness. The fit yields an escape depth of the valence band photoelectrons of about 6 nm. The penetration depth λ_{ph} of the HeI light is about 13 nm [Bez91].

The experimentally determined photoelectron yield was fitted by the equation:

$$P.E.\ yield = A * (1 - \exp(-(\frac{1}{l_{el}} + \frac{1}{l_{ph}}) * thickness)) \qquad 5.5$$

The penetration depth λ_{ph} of HeI light (21.2 eV) into CaF_2 is about 13 nm [Bez91]. The fit gives an escape depth value λ_{el} of 5.8 nm for photoelectrons from the valence band of CaF_2 excited with HeI radiation (21.2 eV).

The second information needed in this section is the electron-phonon scattering lengths for CaF_2. No information on this was found in literature, thus one has to rely on values for other ionic materials. For KBr, the electron-phonon scattering lengths for electrons of 8 eV kinetic energy (roughly corresponding to the kinetic energy of CaF_2 valence band electrons after photoexcitation with HeI radiation) was calculated to be 0.7 nm [AEK92], while for MgO at the same electron energy, a value of about 0.3 nm was determined [FDB85]. As a rough estimate for the electron-phonon scattering lengths in CaF_2, a value of 0.5 nm is taken which means that one photoelectron excites an average of 12 phonons during its travel to the surface.

This large number of electron-phonon scattering events the electron experiences before leaving the crystal has a strong influence on the photoelectron kinetic energy distribution. Since a change of the photoelectron momentum occurs in each electron-phonon interaction, the electron looses any correlation to its initial position in k-space, and the direct transition picture

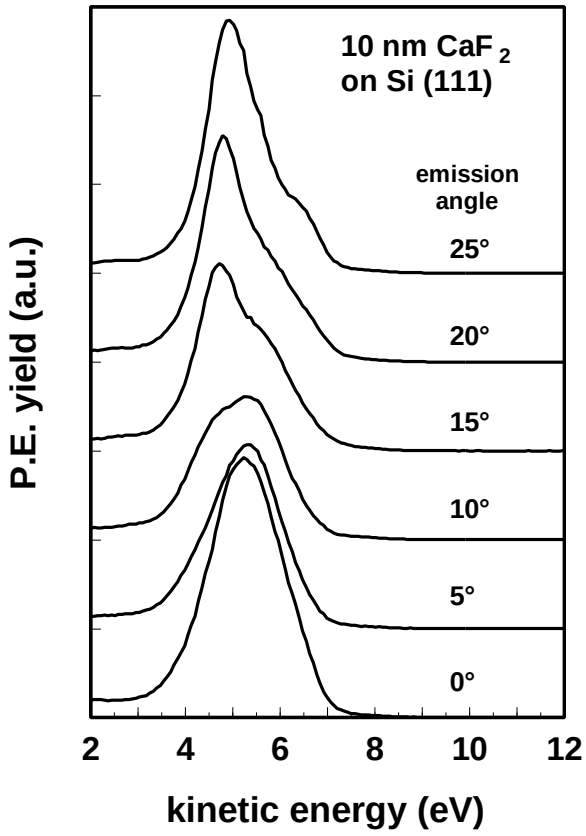

Fig 5.9 Angular dependent photoemission from a 10 nm thick epitaxial film on Si (111).

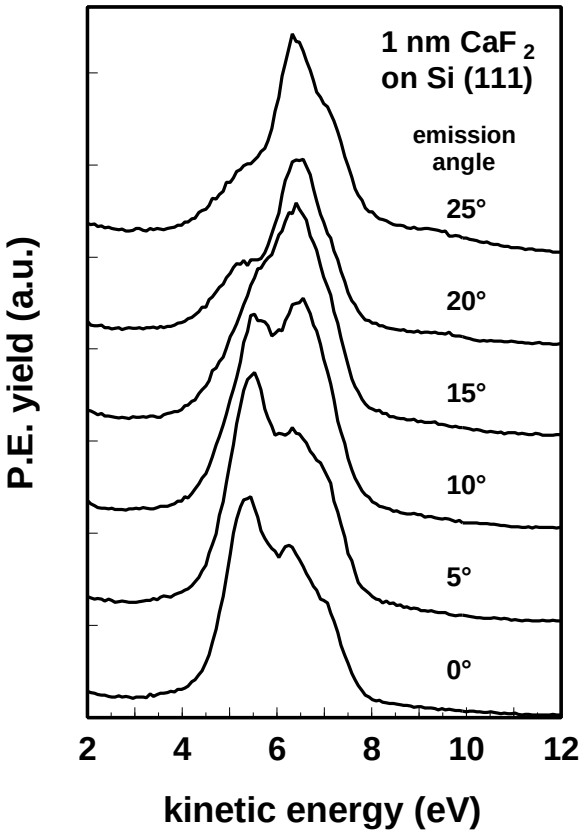

Fig 5.10 Angular dependent photoemission from a 1 nm thick epitaxial film on Si (111).

of photoemission is obscured. The angular distribution of the photoemitted electrons is no longer influenced by the initial state band, but is in fact determined solely by the final state band. However, since the energy lost by the electron in a single phonon excitation is small (some ten meV), the absolute kinetic energy at a certain escape angle is still influenced by the initial state. This process of a direct transition followed by a number of electron-phonon interactions has been referred to as a quasidirect transition [HSt75], [HSt78]. In their investigation of valence band photoemission from NaCl, Himpsel and Steinmann could choose between the direct and quasidirect regime by tuning their photon energy [HSt75]. In the present work, the validity of their model is checked by comparing angular dependent photoemission spectra from an epitaxial film thicker than the escape depth of the photoelectrons on the one side (Fig. 5.9) to those obtained from an epitaxial film with thickness comparable to the electron-phonon scattering mean free path on the other side (Fig. 5.10).

Under 21.2 eV photon irradiation, electrons are excited from the valence band into all available final state bands in the shaded energy interval shown in Fig. 5.2. For a sample that is thick compared to the electron-phonon scattering lengths, the original photoelectron distribution is smeared out. Electrons are interchanged between the bands upon scattering with phonons, resulting in a population of the final state bands that is determined mainly by their density of states. Thus recording normal emission photoelectron spectra from the (111) face of CaF_2, the density of states of the Λ_1-band that is contained in the shaded area of Fig. 5.2 is measured. This is the situation observed in Fig. 5.9, where spectra from a 10 nm thick film are shown.

For a film with a thickness comparable to electron-phonon scattering lengths, only few photoelectrons are interchanged between the final state bands. Discussing as an example the normal emission spectrum in Fig. 5.10, those electrons moving in directions other than the normal emission $\Gamma\Lambda L$ direction leave the crystal without having the chance to be scattered into the $\Gamma\Lambda L$ bands, and those electrons that move in $\Gamma\Lambda L$ direction are not scattered out of this direction. Thus, the original kinetic energy distribution of the photoexcited electrons is preserved. This situation is marked in the band structure Fig. 5.2 by two solid arrows symbolizing transitions from the Λ_1 and Λ_3 valence bands to the Λ_1 conduction band that are both possible for unpolarized radiation (compare dipole selection rules in table 3.2).

The kinetic energy of the valence band photoelectrons measured from the 1 nm film is somewhat higher that for the 10 nm film. This effect was explained by Colbow et al as caused

by tunneling of electrons from the valence band of the substrate into the band gap of CaF_2 [CTR91]. These electrons contribute to the density of states in CaF_2, lowering the binding energy of the F2p valence band electrons.

5.2.5 Photoconductivity during UV irradiation

During photoemission, the CaF_2 samples were heated to avoid charging. Heating activates a conduction mechanism that is investigated in the following section.

Under UV irradiation at elevated temperature, the conductivity was measured during the photoemission experiment by recording the sample current and found to be several orders of magnitude higher than expected for ionic conductivity. As an example, at 520 K, conductivity was about 10^{-8} $(\Omega cm)^{-1}$ compared to an ionic conductivity of 10^{-12} $(\Omega cm)^{-1}$ determined by Svantner and Mariani [SMa78] at the same temperature, but without irradiation. In order to derive the activation energy of the photoinduced conduction mechanism, the variation of the surface potential with temperature was measured. The surface potential U is defined as the difference between the actual peak position $E_{kin}(T)$ at a certain temperature and the "true" peak position E_0 that is measured from the uncharged surface, divided by the electron charge.

$$U = \frac{E_{kin}(T) - E_0}{e} \qquad 5.6$$

A possible way to determine the energy E_0 is the sample bias method described above. A measurement of the temperature dependence of the valence band peak position $E_{kin}(T)$ is shown in Fig. 5.11.

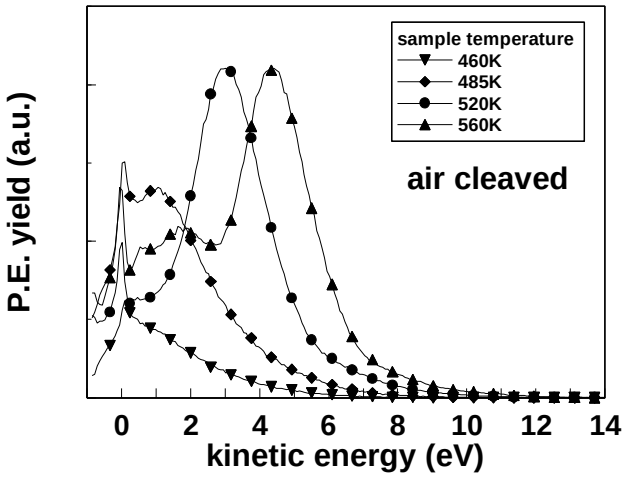

Fig 5.11 Position of the F2p valence band peak dependent on sample temperature. The crystal was cleaved in air. No bias voltage was applied.

A further observation that has to be taken into account when treating the conduction mechanism is the independence of the valence band peak position on UV irradiation intensity. By altering the discharge current of the HeI lamp, the intensity could by changed by a factor of 2. Fig. 5.12 shows spectra taken at maximum and minimum intensity at two temperatures, respectively.

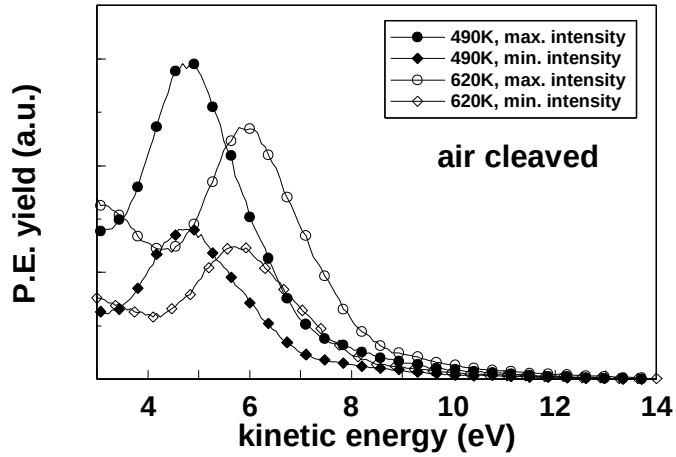

Fig 5.12 Dependence of the surface potential on UV intensity. While the photoelectron yield decreases by a factor of two when switching the discharge current from maximum to minimum value, the peak position does not change.

In the following, a model is developed that accounts for the observed activation energy as well as for the independence of the surface potential from UV light intensity. It is proposed that the conductivity observed during UV irradiation is caused by thermal mobilization of trapped valence band holes (V_k-centers) generated during photoemission. At higher irradiation intensity, proportionally more charge carriers are created.

Within the escape depth of the photoelectrons, photoemission creates holes in the valence band. These valence band holes quickly self-trap and stabilize as V_k-centers due to the strong electron-lattice coupling in CaF_2, a process similar to the selftrapping of excitons described in chapter 2.2. At elevated temperatures these V_k-centers are thermally activated and serve as charge carriers for increasing photoconductivity. The large difference between the ionic conductivity [SMa78] and the one observed in this work during UV irradiation suggests that the current is due to these photo-generated carriers and in first order independent of ionic conductivity. The connection between the photoconductivity σ and the surface potential U can be made by a simple model based on Ohm's law,

$$\vec{j} = \sigma\vec{E} \qquad 5.7$$

where j is the current through the sample and E the electric field across the sample. The positive charge sheet at the surface (the thickness of which is determined by the escape depth of the photoelectrons, which is small compared to the sample thickness) creates an electric field

$$E = U/\varepsilon d \qquad 5.8$$

across the crystal of thickness *d*. The photoconductivity σ can be expressed in terms of the density of holes (V_k-centers), n, generated in photoemission and their mobility μ,

$$\sigma = nq \cdot \mu \qquad 5.9$$

The thermal activation of the V_k-center motion is governed by the Boltzmann distribution determining their mobility. Hence, we can write

$$\sigma = nq \cdot \mu_0 \, exp\{-E_a/kT\} \qquad 5.10$$

where μ_0 is the reference mobility at $T \rightarrow \infty$. The density of charge carriers, n, is an average quantity determined by several factors including the average lifetime of the V_k-centers.
Combining Eqs.(5.7) through (5.10) yields:

$$\frac{U_0}{U} = e^{-E_a/kT}, \qquad 5.11$$

with $$U_0 = \frac{e\ d}{nq} \cdot \frac{j}{m_0}$$

Since the number n of holes generated in photoemission is proportional to the photon flux, an increase in intensity causes a corresponding increase in current density j. The ratio j/nq is therefore constant which means that charging does not depend upon UV-intensity. When using Eq. 5.11, it has to be kept in mind that of course the surface potential can never exceed the value $U_{max} = (\hbar w - W)/e$, where W is the difference between valence band maximum and vacuum potential. When this value is reached, the photon energy is no longer sufficient to remove electrons from the solid against the charge induced field, and the surface potential saturates.

The peak positions $E_{kin}(T)$ shown in Fig. 5.11 are evaluated according to Eq. 5.11 in order to determine the activation energy of the conduction mechanism. For the air cleaved crystal that was used in this photoemission experiment, a value for E_0 of 6.4 eV was measured with the negative bias method. Fig. 5.13 shows that the V_K-center conductivity model well fits the data.

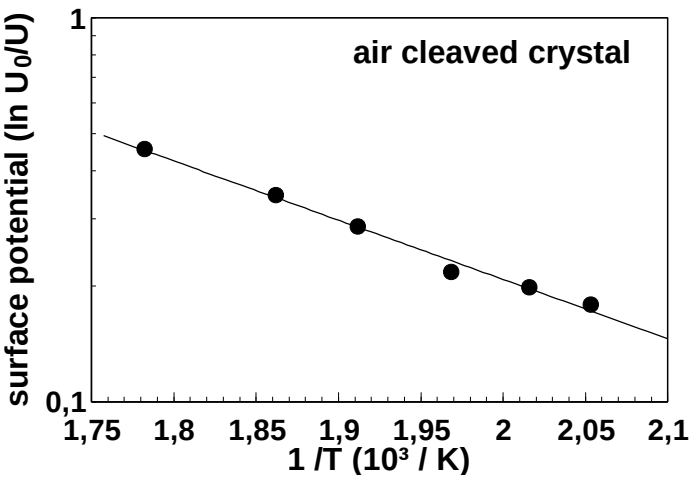

Fig 5.13 Arrhenius graph for the determination of the V_K center activation energy. Sample charging U was derived from a comparison of the actual peak position observed at a certain temperature with those peak positions determined with the negative bias method. The significance of the constant U_0 is explained in the text.

An activation energy for V_K center motion of $E_a = 0.30 \pm 0.06$ eV was derived from Fig. 5.13. The experiment was repeated with a crystal cleaved in UHV where an activation energy of 0.32 eV was determined. The good agreement of the obtained V_K-center activation energy with values given in literature (0.33eV [Ato79]), (0.3 eV [BHK70]) confirms the model.

As a concluding remark, it is mentioned that the conductivity model may also be used "upside down" to determine the energy E_0 for zero surface charge. In this approach, the value E_0 is used as a free parameter that can be adjusted to achieve a best fit to Eq. 5.11. (that means to achieve a linear relation in the Arrhenius graph between 1/T and ln U).

5.2.6 Summary

The features observed in the photoemission spectrum from bulk CaF_2 single crystals cleaved in UHV were described and compared to a band structure calculation and binding energies calculated with the Born model.

It was shown that the interaction of phonons with photoexcited electrons is important for a detailed understanding of the spectra. Creation of phonons during photoelectron excitation results in temperature dependent peak broadening. It was demonstrated that in experiments performed on thick samples with photon energies below the electron-electron scattering threshold, information on the initial state k-vector is lost due to scattering of the photoexcited

electrons with phonons, and the kinetic energy distribution is determined by the final state band density of states only.

It was shown that conductivity during photon irradiation is not ionic, but due to thermally activated V_K-center motion. An activation energy for this conduction mechanism of 0.3 to 0.32 eV was determined, well in accordance with data published in literature.

5.3 Photoemission from differently prepared CaF_2 (111) surfaces

5.3.1 Introduction

This section contains a survey of the electronic structure of differently prepared CaF_2 surfaces, including surfaces produced by cleavage in UHV and in air, surfaces polished with two different techniques, and surfaces of thin epitaxial films evaporated on Si(111). An important issue will be the investigation of bandgap states related to contamination of the crystal during exposure to air.

An influence of impurities caused by exposure of ionic crystals to air on photoemission spectra has been reported occasionally in literature. Pong et al. [PPB80] investigated photoemission from LiF with excitation energies below the valence band threshold. It was found that bandgap states result from exposure to air, while after UHV cleavage, no bandgap emission was detectable. Himpsel and Steinmann [HSt78] noted that NaCl crystals cleaved in air showed a reduced contrast of the angular distribution compared to those cleaved in UHV.

Recently, the topography of contaminated surfaces was directly monitored with the high lateral resolution of a scanning force microscope [Bar98]. On the surface of air cleaved crystals, islands of 5 to some 10 nm size were observed in contrast to the flat topography of UHV cleaved crystals. In the same work, similar islands could be induced on the surface of UHV cleaved crystals by dosage of water and oxygen at room temperature.

In this chapter, similarly prepared CaF_2 surfaces are investigated with UPS, aiming at an understanding of the electronic structure of defects produced by cleavage in UHV and in air as well as by polishing procedures.

5.3.2 Comparison of photoemission from UHV and air cleaved CaF_2 crystals

In this section, bulk crystals with surfaces produced by cleavage in air and in UHV are investigated. The samples were heated to a temperature of typically 550 K to reduce charging. It is shown that air cleaved surfaces are contaminated with impurities causing additional states in the bandgap region of the CaF_2 crystal and surface disorder.

In Fig. 5.14, electron distribution curves (EDC) taken from an air cleaved and a UHV cleaved crystal are shown. The sample was first cleaved in air, transferred into the vacuum chamber and (after bakeout of the UHV system) heated to 800 K for about 30 min to remove as many impurities as possible. The temperature was then lowered to 550 K and the spectrum from

Fig. 5.14 labeled „air cleaved“ was taken. After this measurement was completed, a fresh surface was prepared by cleaving the same crystal in UHV and the spectrum labeled „UHV cleaved“ was recorded.

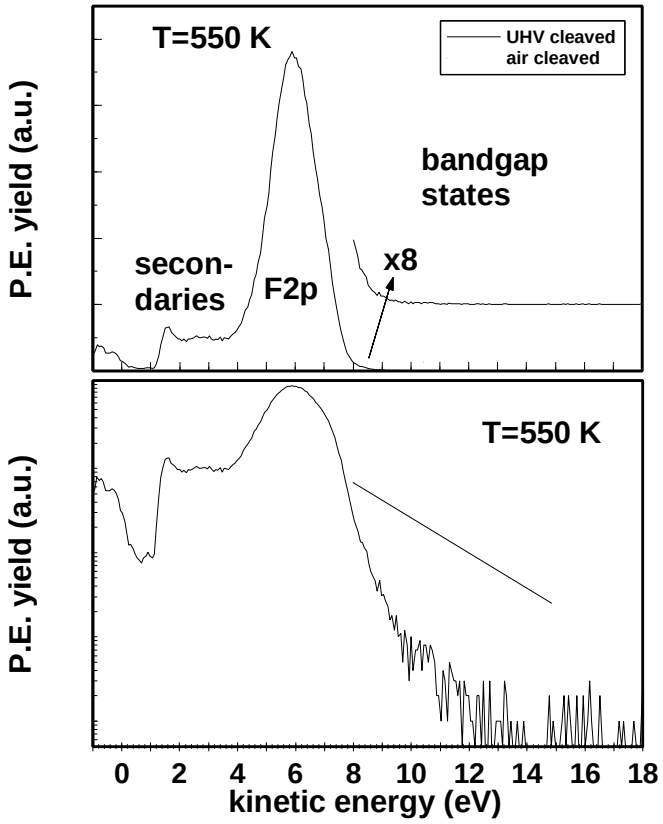

Fig. 5.14 Electron distribution curves taken in normal emission from CaF_2 crystals cleaved in air and in UHV. The HeI line was used for photoexcitation (21.2 eV photon energy). The F2p valence band peak from the air cleaved crystal is broadened, and a considerable number of states in the bandgap is found that extends to about 8 eV above the valence band maximum. These states exhibit an exponential decay towards higher kinetic energies (see line in the lower part of the figure). No distinct oxygen 2p peak is observed, compare to Fig 5.46. Note also the larger secondary electron yield for the air cleaved crystal. In the upper figure, the peak from the air cleaved crystal was shifted by +0.5 eV to allow for a better comparison.

In the EDC from the air cleaved crystal, the F2p valence band peak is broadened towards lower kinetic energies, and a large amount of states in the bandgap is evident from the figure. Much more secondary electrons are observed. For the formation of the impurity related states, it is not necessary to perform the cleavage procedure of the crystal in air, as the same structure was found with a crystal cleaved in UHV, exposed to air for 30 min and then transferred back into UHV. In the logarithmic representation, a rapid decrease of impurity related emission can

be seen at about 15 eV. The energetic distance between the F2p peak and this upper emission limit does not depend on temperature for an individual crystal. (see Fig. 5.15.)

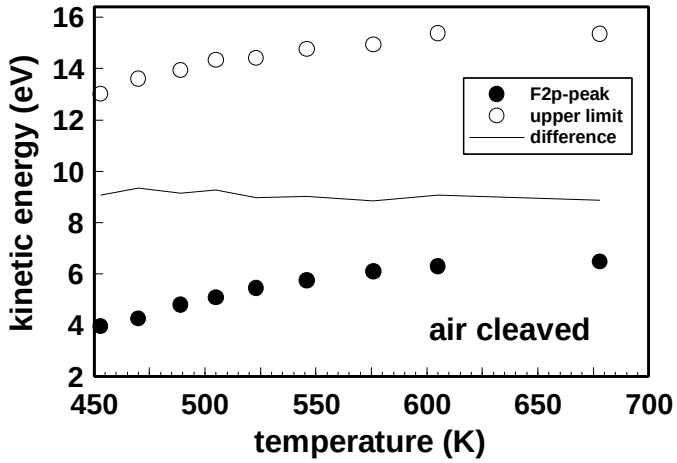

Fig. 5.15 Position of the F2p valence band peak and the impurity related upper emission limit during heating of an air cleaved crystal. The difference between valence band peak and upper limit remains constant during heating. The upper edge of the figure marks the position of the spectrometer Fermi level at 16.4 eV kinetic energy.

However, for different air cleaved crystals, the energetic distance between peak and upper emission limit was not the same as was tested by the measurements shown in Fig. 5.16. It is concluded that the amount or nature of impurities does depend on the individual crystal in

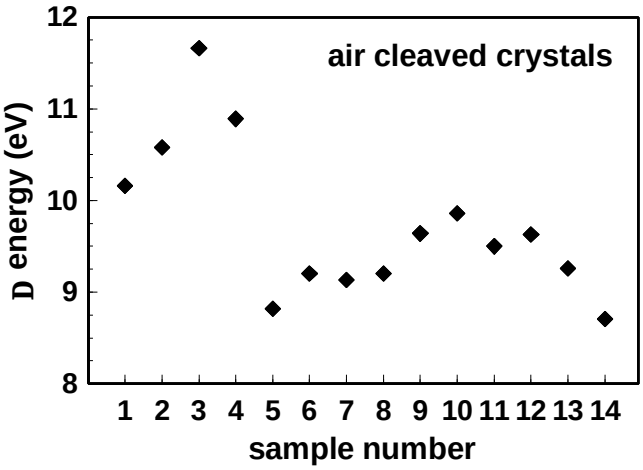

Fig. 5.16 Energy difference between F2p valence band peak maximum and the impurity related upper emission limit for a number of samples. The magnitude of bandgap emission depends on the individual sample. Average of the energetic difference is 9.8 ± 0.8 eV. Spectra were recorded in normal emission at temperatures ranging from 500 to 750 K.

question, for example on the duration of exposure to air and density of steps on which molecules condense.

It was found that heating to temperatures as high as 900 K does not remove impurities. This observation is in contrast to several Auger- and XPS investigations published in literature [SSA87], [SSK92], where it was pointed out that CaF_2 surfaces produced by cleavage in air can be cleaned by heating. The reason for the different observations may be the high escape depth of UPS photoelectrons from insulators compared to XPS and Auger electrons. When the first few Angstroms below the surface were oxygen free after heating, both, XPS and Auger spectroscopy would not detect the impurity, even if deeper layers were still contaminated.

For both UHV and air cleaved surfaces, a series of spectra with different emission angles of the photoelectrons was recorded. Results are shown in Fig. 5.17 for the UHV cleaved crystal and Fig. 5.18 for the air cleaved crystal.

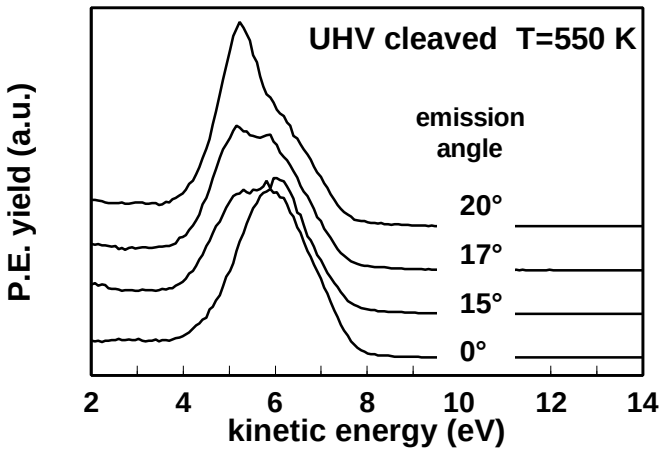

Fig. 5.17 Photoemission spectra taken from a crystal cleaved in UHV. When changing the polar emission angle, intensity effects are observed. For better discernibility, an offset between successive spectra was added.

For the UHV cleaved crystals, two peaks appear with different relative intensities when the emission angle is changed. For the air cleaved crystal, the intensity of a single peak was found to decrease with increasing emission angle, but the shape of the peak did not change.

From the absence of angular effects in the spectra from the air cleaved crystal it is concluded that the surface must be rough on an atomic scale. This conclusion could be confirmed by scanning force microscopy investigations [Ben97], [Bar98]. Photoelectrons passing through

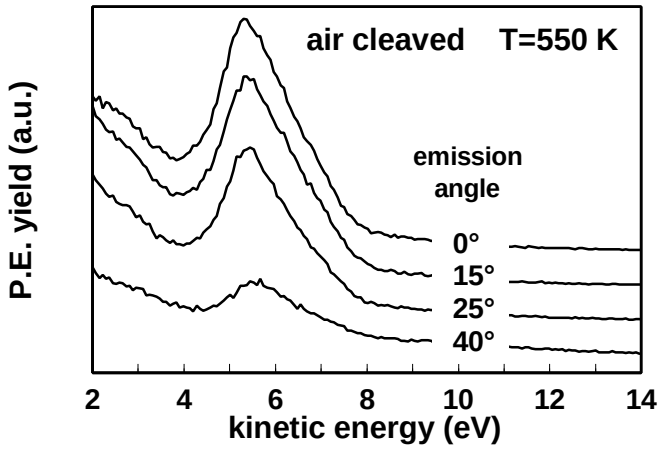

Fig. 5.18 Angular depended photoemission spectra taken from a crystal cleaved in air. The intensity of the valence band peak decreases with increasing emission angle, but the shape of the feature remains the same at all emission angles.

the surface suffer considerable scattering that destroys the original angular distribution. Much more secondary electrons are observed, as the photoelectrons loose energy in scattering events with occupied electronic levels in the bandgap of air cleaved CaF_2.

5.3.3 Photoemission from thin CaF_2 films evaporated on Si(111)

In this section, the findings from UHV cleaved crystals concerning bandgap states and the angular dependence of photoemission are used to check the quality of thin epitaxial CaF_2 films evaporated on Si(111).

In Fig. 5.19, a spectrum from a UHV cleaved crystal is compared with a spectrum taken from a thin epitaxial CaF_2 film. The valence band peak from both samples is identical. In the bandgap of the thin epitaxial film, only a small additional number of states is found compared to the spectrum from the UHV cleaved crystal. It was, however, found that inappropriate preparation conditions like high background pressure during film growth can cause a substantial density of states in the bandgap region, similar to those observed for air cleaved crystals. These bandgap states are presumably due to contamination incorporated into the film during growth. A contribution of photoelectrons from the Si substrate is unlikely, since these electrons have energies above the electron-electron scattering threshold and are therefore effectively damped in CaF_2.

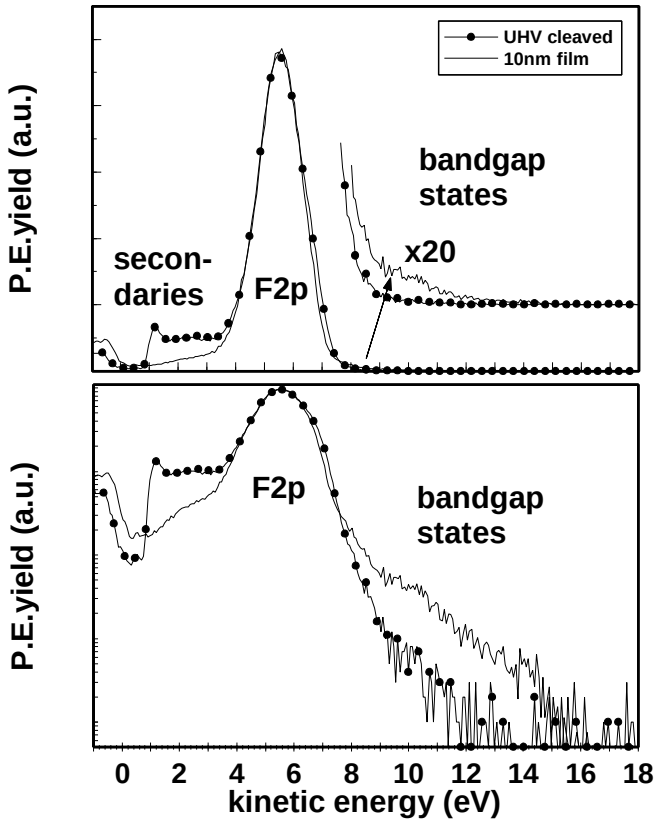

Fig. 5.19 Electron distribution curves taken in normal emission from a CaF_2 crystals cleaved in UHV and a 10 nm epitaxial film evaporated on Si (111). The shape of the F2p valence band peak from both samples is identical. For the thin epitaxial film, only a small number of states in the bandgap is found, however, this number is drastically increased if the background pressure during evaporation is to high. While the UHV cleaved crystal has to be heated to 550 K in order to take a spectrum, the measurement on the thin film was performed at RT. Spectra were normalized to the same height, the one from the UHV cleaved crystal was shifted by 0.3 eV to lower kinetic energy.

Also for a thin epitaxial film, a series of photoemission spectra recorded at different emission angles is shown in Fig. 5.20. It can be seen that the angular dependence closely resembles that of the UHV cleaved crystal shown in Fig. 5.17. The somewhat less pronounced features found in the spectrum from the crystal may be due to a slight residual charging. It is concluded that the electronic structure of thin epitaxial films evaporated on Si (111) and UHV cleaved crystals is equivalent as far as photoemission studies are concerned. For some investigations, amorphous films that were evaporated on SiO_2 instead on Si(111) 7x7 were produced. These films did not show the angular dependent intensity effects that are visible in Fig. 5.20.

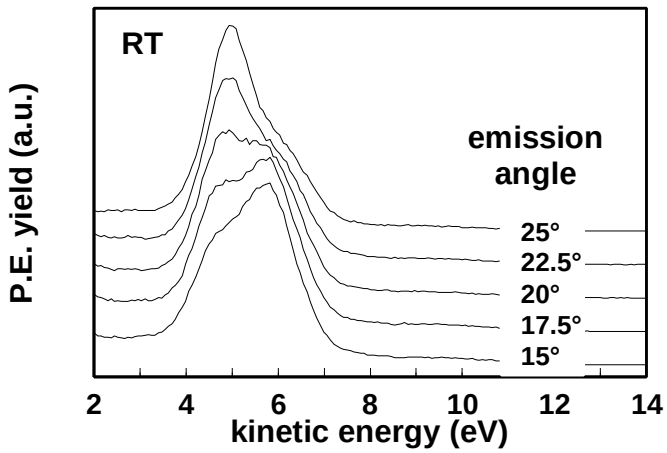

Fig. 5.20 Series of photoemission spectra obtained from a 5 nm thick CaF_2 film evaporated on Si (111). Note that these spectra were taken at room temperature (RT). The angular effects are similar to those observed on UHV cleaved crystals.

No dependence of the valence band peak position on the film thickness was observed at room temperature for film thicknesses ranging from 2 to 36 nm (Fig 5.21).

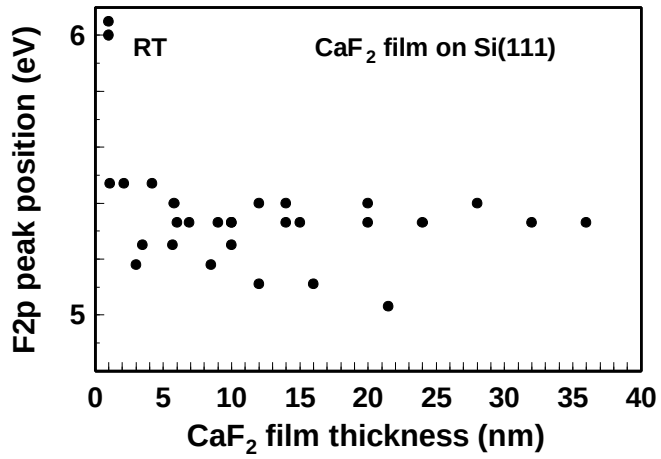

Fig. 5.21 Position of the valence band peak maximum for CaF_2 films of different thickness evaporated on Si (111). No charging is observed up to the highest investigated film thickness of 36 nm. The average of the peak position is 5.3 ± 0.1 eV. Spectra were taken at room temperature.

For very thin films, somewhat higher photoelectron energies were observed, as was already discussed at the end of section 5.2.4.

The observation made here that even films of 36 nm thickness are not charged can be understood within the V_K center conductivity model that was presented in section 5.2.5. The magnitude of charging that is to be expected in typical experimental situations during the investigation of films or crystals can be estimated using Eq. 5.11:

$$\frac{U_0}{U} = e^{-\frac{E_a}{kT}} \text{, where } U_0 = \frac{e\ d}{nq} \cdot \frac{j}{m_0} \qquad 5.11$$

For thin films, the thickness d is of the order 10 nm instead of roughly 1 mm for crystals, and in the above experiments on thin films (Fig 5.21), the temperature of the sample during a typical photoemission experiment was 300 K instead of about 600 K as it was during photoemission of crystals. Taking E_a = 0.32 eV, charging is about 3 orders of magnitude smaller for a 10 nm film at 300 K than for a 1 mm thick crystal at 600 K. At 150 K, however, Eq. 5.11 predicts strong charging also for a 10 nm film, which is not observed experimentally (compare below Fig. 5.36). In films thinner than the penetration depth of the UV-photons, there is an additional conduction mechanism due to photoexcited conduction band electrons that does not depend on temperature.

Occasionally, in the photoemission spectra recorded from thin films, distinct peaks were found in the bandgap region. Examples of spectra containing theses states are shown in Fig. 5.22.

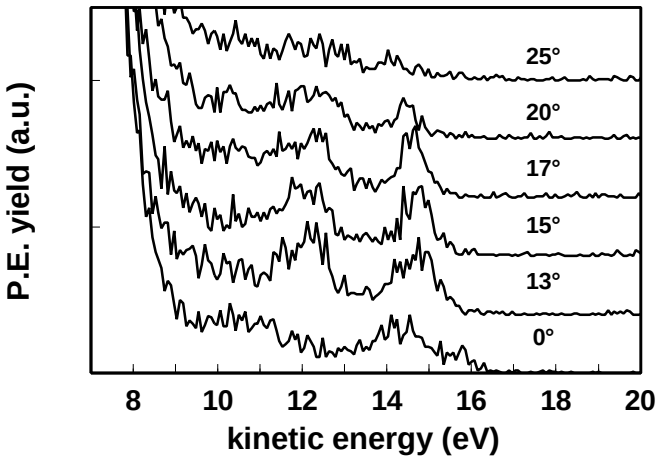

Fig. 5.22 Photoemission spectra taken from a 10 nm CaF_2 film at various emission angles. The intensity ratio between F2p valence band peak (at 5.3 eV) and the defect peak at 14.3 eV in normal emission is 825 : 1. Temperature was RT.

Depending on the individual film, the observed emission was more or less strong, compare the normal emission spectrum in Fig. 5.22 to the one shown in Fig. 5.19 where the peak at 10.9 eV does not appear, while the one at 14.5 eV is very faint. The sample was not irradiated, except for the time necessary to record the spectra which took 5 min each.

In the normal emission spectrum shown in Fig. 5.22, the positions of the two bandgap features are 5.6 eV and 9 eV above the valence band peak maximum. The feature with lower kinetic

energy probably reflects the first stages of surface oxidation due to a reaction with residual gas, while the structure 9 eV above the valence band peak maximum is assigned to the ground state of the bulk *F*-center. Adding 9 eV to the position of the valence band peak maximum in Fig. 5.4 (right hand side), one arrives at a *F*-center ground state level positioned at -2 eV in the energy scale of Fig. 5.4, i.e. 2 eV below the vacuum level and 3.6 eV below the conduction band minimum. These energetic levels are summarized in Fig. 5.23.

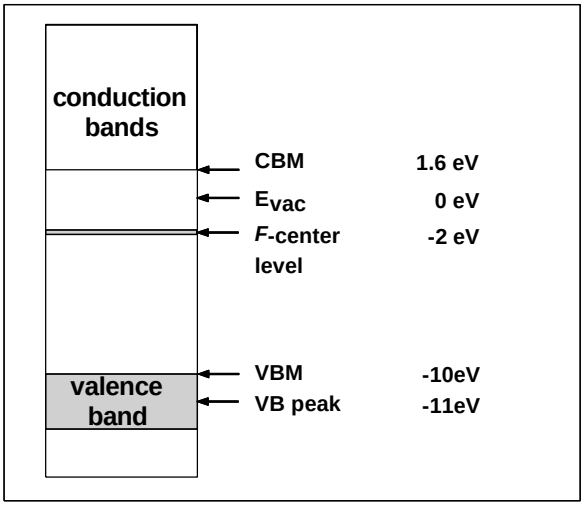

Fig. 5.23 Energy level diagram for the *F*-center state measured in Fig. 5.22. VBM and CBM denote the valence band maximum and conduction band minimum, respectively.

The absolute *F*-center level position determined with UPS corresponds well with photoemission results published by Karlson et al [KHM86], who found the ground state level of the *F*-center at 8.3 eV above the valence band maximum, and with a theoretical calculation by Westin et al [WRM90], were a ground state of the *F*-center level of 2 eV below the vacuum level was predicted. The relative position of the levels in Fig. 5.23 can be compared to the excitation energy of the *F*-center of 3.3 eV determined with optical spectroscopy [CHH69], and with the excitation energy of the surface *F*-center of 1.8 eV measured with EELS [SSA87]. These energies correspond well with the energy scale of the *F*-center that was determined here (Fig 5.23). The excitation energy of 3.3 eV is assigned to an excitation from the *F*-center ground state into a bound state slightly below the conduction band minimum, while the excitation energy of 1.8 eV is assigned to a transition of the *F*-center electron from the ground state into the vacuum, which is possible when the *F*-center is located at the surface. This latter assignment is different from the one made originally by the authors of the EELS investigation [SSA87], who assumed that the energy loss peak at 1.8 eV corresponds to a

transition of a surface *F*-center electron into the conduction band. It is concluded that *F*-center excitation energies published in literature fit well into the level diagram determined with photoemission, which confirms the assignment of the structure found at 14.3 eV in Fig. 5.22 to the *F*-center.

The *F*-centers observed here may origin from an additive coloring during thin film preparation caused by a certain concentration of calcium-monofluoride in the molecular beam. During film preparation, CaF_2 evaporates as a molecule, thus a-priori solving stoichiometric problems. However, depending on the evaporation technique, this is not exactly true. In an electron beam evaporator a certain fraction of the evaporating CaF_2 molecules is broken up in CaF and F by electrons of several 100 eV that are used for heating the crucible. Depending on the technical conditions inside the evaporator, the resulting additive coloring can be more or less strong which explains the varying intensity of the bandgap feature observed for different films.

5.3.4 Gas dosage to CaF_2 surfaces

In order to reveal the chemical nature of the bandgap emission from air cleaved crystals, different gases were dosed to UHV cleaved crystals and thin CaF_2 films. No effect was observed after dosage of N_2, CO_2, and H_2O at 550 K to crystals and at RT to thin films. Only after dosage of oxygen, the bandgap emission did increase as is shown in Figs. 5.24 and 5.25.

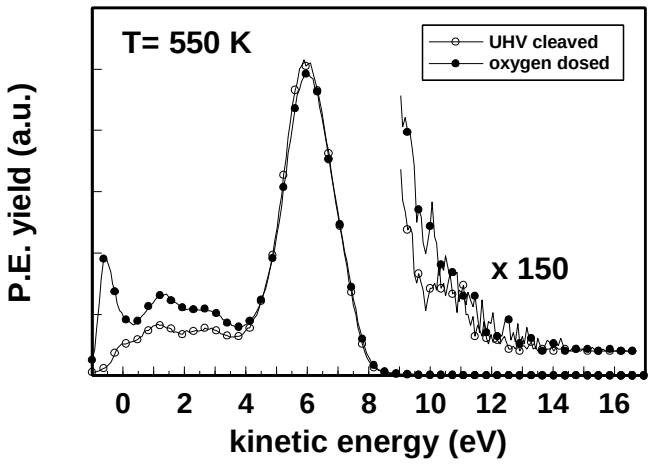

Fig. 5.24 Oxygen at a pressure of $5*10^{-8}$ mbar was dosed for 120 min to an UHV cleaved sample at a temperature of 550 K. The first spectrum was measured before dosage. During exposure, the sample was not irradiated with UV light. The second spectrum was taken after dosage. The oxygen induced structure is similar to the bandgap emission observed in the spectra from air cleaved crystals, however, it is much smaller in intensity. The spectrum taken after oxygen dosage was shifted by 0.75 eV to lower kinetic energies.

Care was taken not to irradiate the crystal with UV photons during dosage. Also, no filaments were in line of sight with the sample, excluding any contribution from atomic oxygen to the adsorption process. The spectrum taken after oxygen dosage is distinguished from the one taken from the pristine surface by a higher density of states in the bandgap and an increased true secondary electron emission. From the similarity of the bandgap states distribution that is observed after oxygen dosage to those observed after exposure of the of the crystal to air, it is concluded that mainly oxygen causes the bandgap states of air cleaved crystals. This hypothesis is further supported below, where the results of electron irradiation experiments are presented.
However, the effect is much smaller for the oxygen dosed than for air cleaved samples, which is reasonable as the total exposure was just 360 L (L = Langmuir = $1s*10^{-6}$ mbar) compared to $3.6\ 10^{11}$ L for the crystal that was exposed to air (assuming a partial pressure of O_2 of 200 mbar for 30 min). The higher population of the true secondary electron states after oxygen dosage is interpreted as related to increased electron-electron scattering at the adsorbate induced bandgap states.
It can be seen in Fig. 5.25 that, unlike for air cleaved samples, the angular dependence of the spectral features of the UHV cleaved crystal was not disturbed by exposure to 360 L oxygen, which is reasonable from the much lower dosage compared to air cleaved crystals.

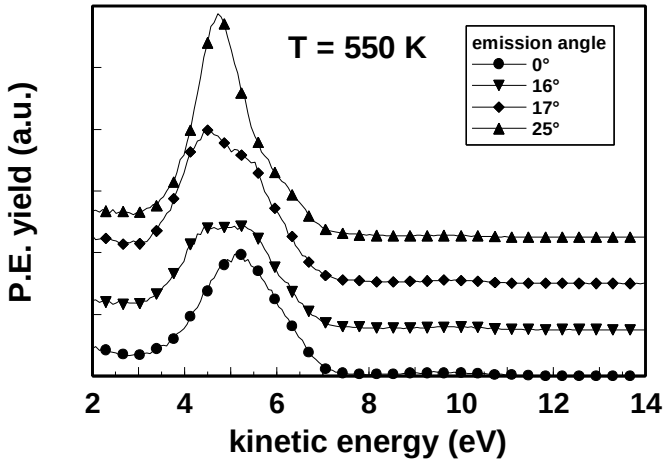

Fig. 5.25 Angle dependent photoemission spectra from a UHV cleaved sample that was dosed with $5*10^{-8}$ mbar for 120 min at 550 K. Angular dependence did not smear out as was observed for crystals cleaved in air.

A similar oxygen dosage experiment as performed with the UHV cleaved crystal was repeated with a thin epitaxial CaF_2 film on Si(111) at RT (Fig 5.26).

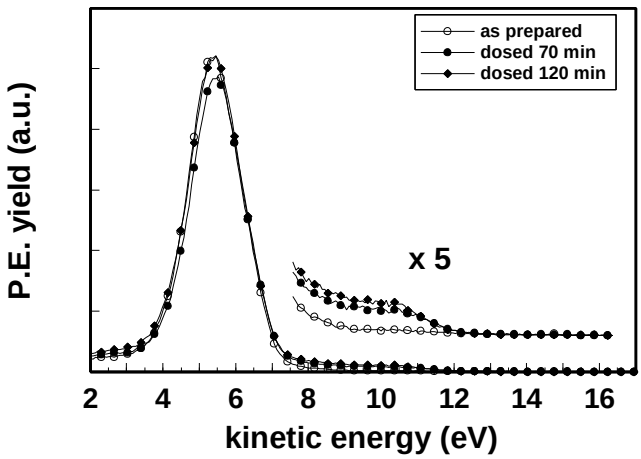

Fig. 5.26 Oxygen dosage of a 10 nm CaF_2 film without UV irradiation during dosage. Oxygen pressure was $5*10^{-9}$ mbar, the experiment was performed at RT.

Although, the thin film was dosed with only 36 L of oxygen, compared to 360 L for the crystal, the bandgap emission appears to be much more pronounced. This difference is interpreted as a hint on oxygen diffusion into the bulk of the samples. In crystals, oxygen penetrates into deeper layers, reducing the concentration at the surface. This process is expected to be further enhanced when working at elevated temperature as was done in the case of the crystal (550 K instead of RT). With films, there is only a very limited volume for oxygen to diffuse, and consequently a higher concentration of the impurity remains near the surface within the probe depth of UPS results.

The chemical nature of the bond that is established between CaF_2 and oxygen is somewhat puzzling. On the one hand, oxygen is not chemisorbed, otherwise a O2p peak would show up in the spectrum as was calculated by V. Puchin [PPH98a] (see Section 5.4.6). Also for energetic reasons, it is unlikely that oxygen replaces fluorine.

On the other hand, oxygen impurities on air cleaved crystals could not be removed by heating to temperatures up to 900 K, indicating that oxygen is stronger bound than common in physisorbed systems at ionic surfaces [FUm93]. It is proposed that oxygen is not only adsorbed on the surface, but also dissolved in the lattice of CaF_2. It cannot be distinguished with UPS whether it is present in molecular form or if dissociation into atomic oxygen occurs, since no distinct peaks that can be related to oxygen are visible in the spectra. Emission from oxygen states is likely to be hidden in the valence band signal from CaF_2, as is concluded from Fig. 5.27, where the first ionization potential of atomic and molecular oxygen [Wea74] is

schematically compared to the measured level diagram of CaF_2 from Fig. 5.4. A contribution from the Madelung potential to the binding energy was neglected in this figure.

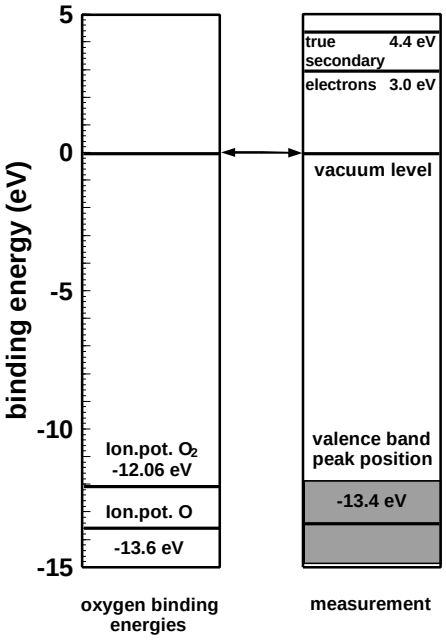

Fig. 5.27 Schematic energy level diagram comparing atomic and molecular ionization potential of oxygen [Wea74] to photoemission results from CaF_2 crystals cleaved in UHV. The shaded area marks the approximate valence band width of the F2p peak, which was assumed to be 3 eV. From the relative positions of the levels, it is concluded that the emission from the oxygen states is masked by F2p valence band emission.

Assuming the impurities reside in the interstitial sides of the fluorine lattice (compare Fig. 2.1), the binding energies shown in Fig. 5.27 may be shifted upwards by about 0.5 to 1 eV. The position of the level related to molecular oxygen is near the valence band maximum, and photoemission from such states may account for the broadening of the F2p valence band peak that can be seen in the spectrum from the air cleaved crystal shown in Fig. 5.14. Adsorption of water on thin CaF_2 films was not observed at RT, however, the situation changed when cooling the film. In Fig. 5.28, spectra taken during cooling of a 3 nm thick epitaxial CaF_2 film exposed to a constant water vapor pressure of $5*10^{-8}$ mbar are shown. When the sample temperature drops below about 153 K at a pressure of $5*10^{-8}$ mbar, drastic changes in the spectra are observed, indicating that water has adsorbed on the surface. The process is reversible, after heating, water desorbs and the spectrum of CaF_2 becomes visible again. In the experiments, water adsorption was generally observed at a somewhat higher temperature than indicated by the vapor pressure curve of solid ice, indicating that the interaction of water vapor

with CaF_2 is stronger than with ice. Whether this is an intrinsic property of the CaF_2 surface or related to defects could not be determined.

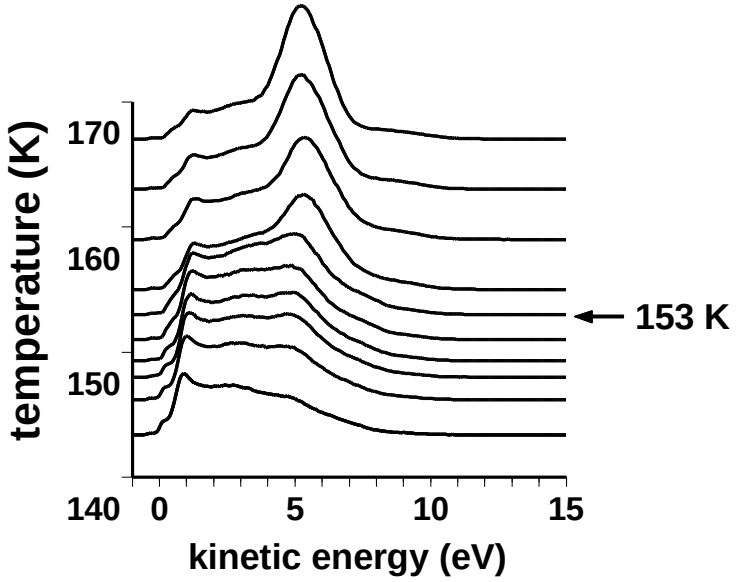

Fig. 5.28 Normal emission spectra taken during water dosage of a 3 nm CaF_2 film evaporated on Si(111). The experiment was performed at a constant water pressure of $5*10^{-8}$ mbar, while the sample was cooled down. After water adsorption, which starts at about 153 K, very broad and structureless features are observed in the spectrum.

5.3.5. Photoemission from polished surfaces

From a technological point of view, it was interesting to investigate whether additional states in the bandgap are caused by polishing procedures. Earlier work performed in our group was concerned with the closely related subject of laser damage thresholds of optical materials [JGS95], [GSJ96], [SGS97], [Ste97]. It was assumed that observed differences in laser damage thresholds between air cleaved (on terraces up to 40 J/cm^2 at 248 nm) and standard polished CaF_2 crystals (10 J/cm^2 at 248 nm) [Gog96] are related to additional states in the bandgap of the polished crystals.

Two types of polished crystals were compared in this UPS investigation, a crystal that was polished with a standard hard polishing procedure, and a "super polished" crystal surface prepared by diamond turning.

In Fig 5.29, photoemission spectra from a UHV cleaved, an air cleaved crystal and the diamond turned crystal are compared.

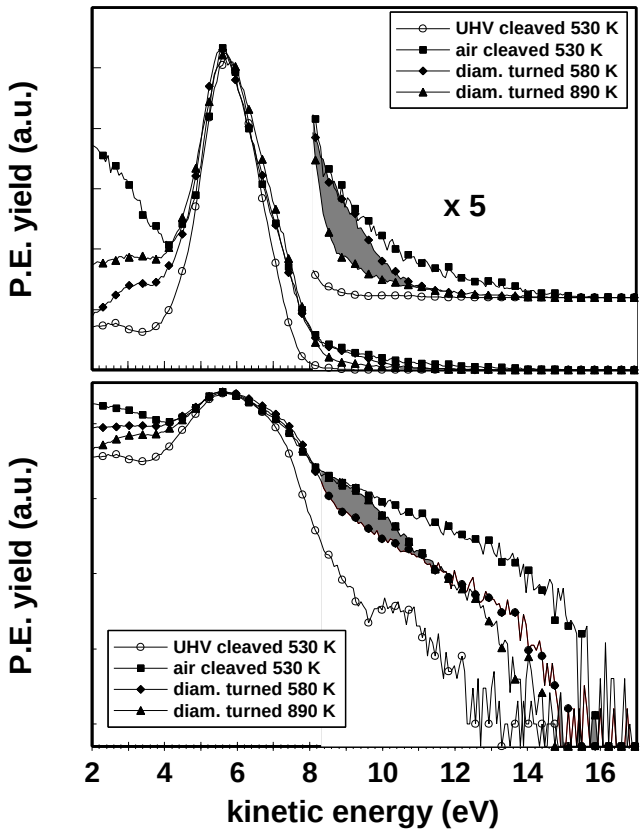

Fig. 5.29 Photoemission spectra taken from a UHV cleaved, an air cleaved, and a diamond turned CaF_2 crystal. The diamond turned sample was also heated to 890 K to remove as many impurities as possible. The bandgap emission could be reduced by heating (shaded area). However, the broadened and asymmetric shape of the valence band did not change. From a comparison with the calculations presented in chapter 5.4.6, it is concluded that OH^- impurities that desorb or diffuse into the bulk at high temperature are responsible for some of the states observed in the spectra from the diamond turned crystal. Spectra were normalized to the same height and shifted to the same position.

The spectra from the air cleaved crystal shows a tail of occupied states extending to about 7 eV into the bandgap. Photoemission spectra from the diamond turned crystal are shown at two different temperatures. Compared to air cleaved crystals, the density of states in the bandgap is reduced. The diamond turned crystal seems to be polluted with water that is present on the surface in form of OH^- (comp. Fig 5.46). Upon heating, the OH^- peak is reduced, which may be either due to desorption or due to a reaction at the surface:

$OH^- + F^- \Rightarrow O^{2-} + HF$, where the O^{2-} bounds to calcium. It may also diffuse into the bulk [MAw68].

Four spectra from different standard polished crystals and from the diamond turned crystal are compared in Fig. 5.30.

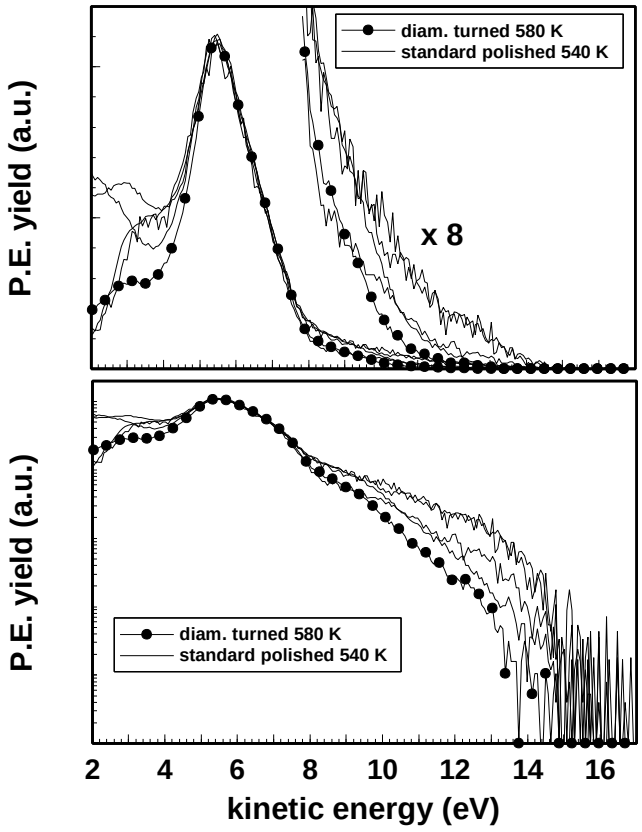

Fig. 5.30 Photoemission spectra taken from a diamond turned and four standard polished CaF_2 crystals. The spectrum from the diamond turned crystal was taken before heating to 890 K, it corresponds to the curve recorded at 580 K in Fig. 5.29.

Considerable differences in the bandgap density of states are observed for the different standard polished crystals shown in Fig. 5.30. Compared to these samples, the diamond turned crystal exhibits the lowest density of states. However, it seems that the most important contribution to the bandgap density of states is induced simply by the unavoidable exposure of polished crystals to air and water. Advanced polishing techniques seem to reduce the density of bandgap states.

5.3.6 Summary

It was shown that exposure of CaF_2 crystals to air causes a high amount of bandgap states, and surface order is lost. It was not possible to clean surfaces prepared by cleavage in air just by heating in the investigated temperature interval up to 900 K.

Dosage of different gases to UHV cleaved crystals revealed that the impurity that is most important for the formation of the bandgap states is oxygen. In spite of the high thermal stability of oxygen on CaF_2 that was observed, no photoemission features expected for oxygen chemically bound to calcium where found. It was concluded that oxygen diffuses into the lattice of CaF_2. Water was observed to adsorb only at low temperatures.

Thin films were found to have photoemission properties very close to those of UHV cleaved crystals. No surface charging during UV irradiation at RT was observed up to the highest investigated film thickness of 36 nm.

An influence of polishing techniques on the bandgap density of states was investigated, however, the predominant contribution to impurity related states seems to arise from exposure to air.

5.4. Irradiation induced effects in CaF_2

5.4.1 Introduction

When CaF_2 is exposed to ionizing radiation, desorption of fluorine and an enrichment of the crystal with calcium metal is observed, as was discussed in detail in section 2.3.

Several reports have been published on the electronic structure of radiation induced defects on the CaF_2 surface. Karlson et al [KHM86] investigated UV photon (36 eV) induced changes of thin CaF_2 films evaporated on Si(111). An irradiation induced feature 0.5 eV below the Fermi level of the substrate was found. The structure was metastable, it disappeared when leaving the sample unirradiated for some hours or after flash annealing to 970 K. As a tentative explanation, the new structure was assigned to an ordered array of surface *F*-centers formed after photon stimulated desorption of fluorine. If this explanation was true, a very high efficiency for this process follows, as only about 10^{15} photons of 36 eV were needed to desorb the $8*10^{14}$ surface fluorines.

Saiki et al [SSA87] investigated electron beam induced structures in the band gap region of CaF_2 crystals with electron energy loss spectroscopy (EELS) using 150 eV electrons. During the first stages of irradiation, a loss peak at 1.8 eV appeared that saturated at a dose of about $1.5*10^{15}$ electrons/cm^2. Following the ideas presented in the work of Karlson et al, the authors assumed that surface *F*-centers are formed during electron stimulated fluorine desorption. The structure was assigned to a transition of the surface *F*-center electron into the conduction band. With continuing irradiation, a loss peak at 3.4 eV appeared for dosages larger than 400 µC/cm^2, which was assigned to surface plasmons in Ca colloids. For dosages exceeding 4 mC/cm^2, a broad structure at 8 eV was observed that was interpreted as the Ca colloid volume plasmon. In summary, the work of Saiki et al indicates that under irradiation with electrons of 150 eV primary energy, first an ordered structure of *F*-centers is produced by fluorine desorption. This stage is followed by an aggregation of Ca atoms that remain on the surface of the crystal after fluorine has desorbed. With increasing electron dose, the metallic aggregates grow larger. The picture of colloids growing on the CaF_2 (111) surface after electron irradiation was also confirmed with scanning force microscopy [RWB96], [BRM97].

In the present chapter, similar aspects of electron and photon irradiation induced changes of the electronic structure of CaF_2 are investigated with UPS. Additionally, beam induced reactions of oxygen with irradiated surfaces are analyzed. The results are compared to a theoretical calculation.

5.4.2 Electron irradiation effects at high temperature

The electronic structure of CaF_2 (111) surfaces was altered by irradiation with 1.5 to 2.5 keV electrons. Significant differences between results from UHV and air cleaved samples were found. In the previous chapter, the bandgap states observed in the spectra from air cleaved crystals were assigned to oxygen that was assumed to be dissolved in the bulk of CaF_2. In this section, oxygen is shown to have an important influence on the formation of irradiation induced bandgap states.

At the beginning of this section, the response of UHV and air cleaved crystals to electron irradiation is compared. A temperature of 400 K during irradiation was chosen to ensure efficient metal production. Fig. 5.31 shows two spectra from a UHV cleaved crystal before and after 1.5 keV electron irradiation.

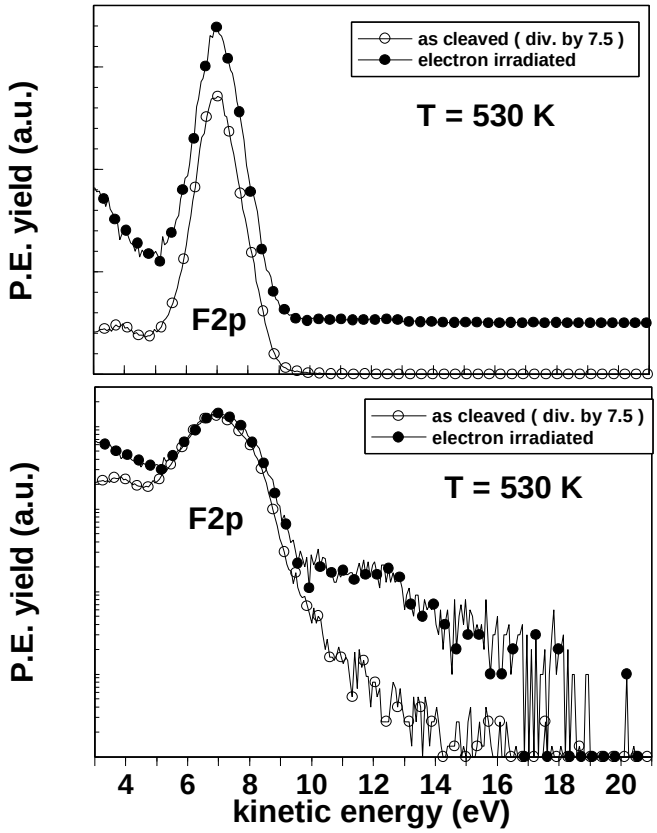

Fig. 5.31 Ultraviolet photoelectron spectra of a CaF_2(111) crystal cleaved in UHV and irradiated at 400 K with 144 mC/cm^2 of 1.5 keV electrons. In spite of the high irradiation dosage, only a small density of bandgap states was observed, but the valence band emission has decreased strongly. For a better representation, the photoelectron yield for the unirradiated surface was divided by a factor of 7.5, and the spectrum from the unirradiated crystal was shifted by 2.6 eV towards higher kinetic energy. In the upper (linear) part of the figure, an offset was added to the spectrum to allow for better comparison.

The lower curve in the linear part of Fig. 5.31 shows the photoelectron spectrum for the as-cleaved surface with a small density of states in the band gap. The upper curve represents a spectrum measured after electron irradiation with a dosage of 144 mC/cm^2 at 400 K. This dosage corresponds to the irradiation of 1000 electrons per surface lattice site. A decrease in fluorine 2p emission by a factor of 7.5 is observed. This decrease is unexpectedly large compared to Auger spectroscopy results published in literature. After irradiation of 18 C/cm^2 (i.e. more than 100 times the dosage applied in this measurement) of 2.5 keV electrons on the CaF_2 surface, Baunack and Zehe [BZe90a,b] found a decrease in fluorine signal intensity by a factor of about 2, similar observations were made by Strecker et al, where the fluorine signal decreased by the same factor after a dosage of 7 C/cm^2 [SMG81]. The strong decrease observed with UPS after irradiation is thus not believed to reflect fluorine depletion only, but mainly a strongly reduced photoelectron escape depth. While photoelectrons excited with HeI radiation in undamaged CaF_2 crystals have kinetic energies below the electron-electron scattering threshold, the situation changes in the presence of a large number of defects in the bandgap. Now, energy can be lost in scattering events with defect levels or calcium metal clusters. From the valence band photoelectron yield before and after electron irradiation, an escape depth of about 0.8 nm for F2p electrons in the damaged crystal is estimated.

In spite of the strong decrease in valence band photoelectron yield, only very small radiation induced changes in the band gap were found, and no step that could be identified as the Fermi level of metallic calcium was observed. On the surface, a gray film has formed that can be seen with the bare eye. In an ex-situ resistivity measurement, the gray film was found to be conductive, which assures that indeed metallic calcium was present.

The lack of photoemission signal from calcium is assigned to the very low cross section for excitation of s-like levels with photon energies in the UPS regime [Wil77]. The insensitivity of UPS with HeI excitation to metallic calcium states was demonstrated in a recent photoemission study by Ochs et al [OBK98], who performed simultaneous measurements with metastable impact emission spectroscopy (MIES) and UPS (HeI). In MIES, the emitted electrons originate from metastable He*(2^3S) interacting with the surface via an Auger deexcitation process. MIES is thus not restricted to optical selection rules. In the study, it could be shown with MIES that metallic calcium was indeed produced by 1486 eV X-ray irradiation, however, at the same time, no calcium states were observable with UPS. A similar failure to detect s-like alkali metal states by HeI photoexcitation was also encountered in studies of alkali metal adsorption on metallic substrates [HHS88]. For the present work, it is thus concluded that

there is no contradiction between the ex-situ observation of a conducting film on the irradiated crystal and the lack of photoemission signal.

The presence of metallic calcium in the electron irradiated crystal shows up indirectly via a shift of the F2p valence band position towards higher kinetic energy. The magnitude of the shift is shown Fig. 5.32 as a function of the irradiated electron dose.

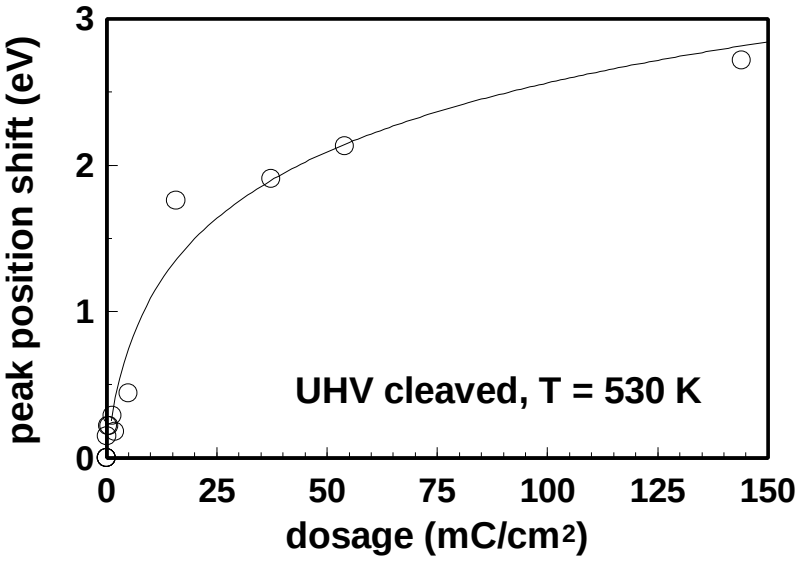

Fig. 5.32 Shift of the F2p valence band peak position towards higher kinetic energy after electron irradiation. Temperature during measurement was 530 K. The solid line represents a fit to the data by a logarithmic function.

In literature, similar shifts of the valence band peak kinetic energy were observed when depositing increasingly thick metallic overlayers on CaF_2 [XVW89]. It was assumed that a dipole layer builds up at the metal-insulator interface to accommodate the vacuum level discontinuity at the interface.

The photoemission spectra taken after electron irradiation from crystals cleaved in air were quite different from those taken from UHV cleaved crystals. Spectra from an air cleaved crystal before and after irradiation with 2.5 keV electrons are shown in Fig. 5.33. Upon electron irradiation, the fluorine 2p valence band emission intensity decreases like it was observed after irradiation of UHV cleaved crystals, however, different from the results shown in Fig. 5.31, a new feature 5.8 eV above the valence band peak maximum emerges. The new feature starts to saturate at an electron dosage of roughly 0.1 C/cm^2, as can be seen in Fig. 5.34 where the integrated photoemission intensity of the new peak is shown as a function of the electron irradiation dose.

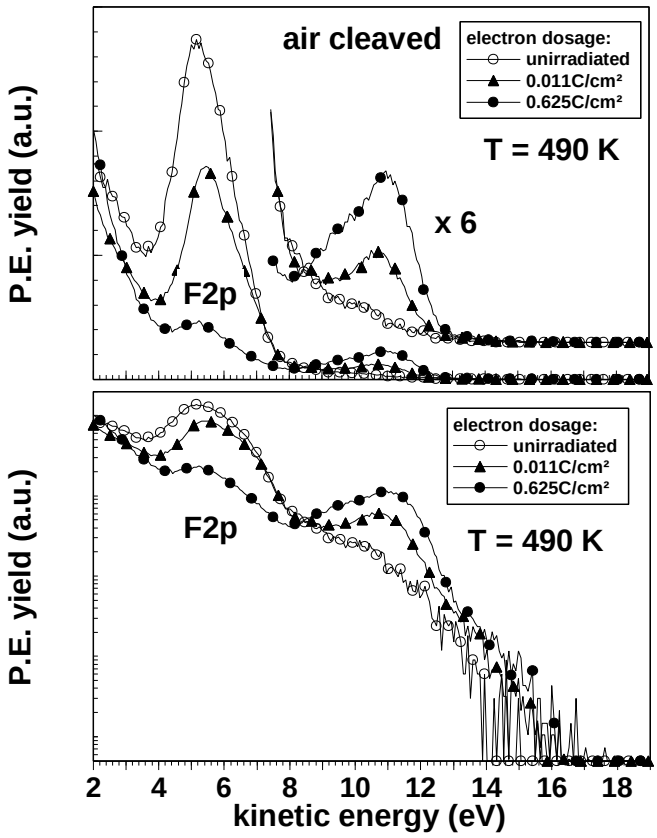

Fig. 5.33 Ultraviolet photoelectron spectra of CaF_2(111) as cleaved in air and after irradiation with two dosages of 2.5 keV electrons at a current density of 180 μA/cm^2. Sample temperature was 400 K during irradiation and 490 K during UPS measurements. With increasing dosage the F2p intensity decreases while the O2p peak emerges. (spectra have not been shifted)

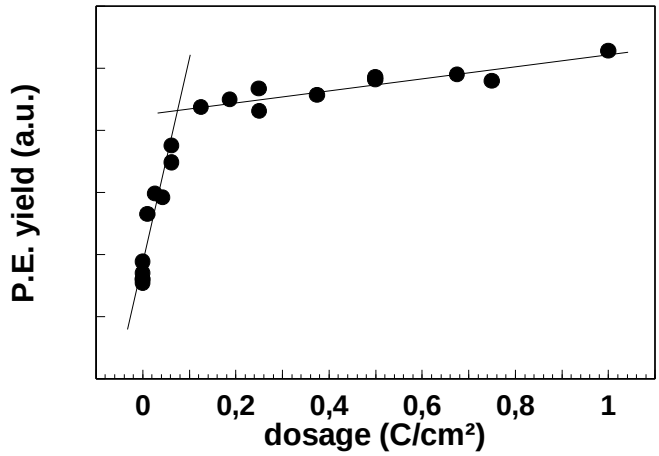

Fig. 5.34 Intensity of the bandgap feature dependent from the electron dosage. For each point, a fresh spot on the crystal was irradiated. A two step behavior is found: in the low dose region, a steep increase of the signal occurs, which ends at roughly 0.1 C/cm^2. From there to the maximum dosage of 1 C/cm^2, only a slight further increase is observed. Primary energy was 2.5 keV at a current density of 180 μA/cm^2. Temperature during electron irradiation was 400 K, the UPS measurements were performed at 490 K.

From a comparison with results measured with optical absorption spectroscopy [Bou97], it is concluded that the bending of the curve in Fig. 5.34 at a dosage of 0.1 C/cm^2 is not due to saturation of the metallization efficiency. Bouchaala [Bou97] found a linear increase of metal production under electron irradiation up to a dosage of 0.27 C/cm^2, while at higher dosages, metallization became less efficient.

To explain the photoemission result shown in Fig. 5.34, it is proposed that at a dosage of 0.1 C/cm^2, all the oxygen that is dissolved in the lattice within the probe depth of the photoelectrons has reacted with the calcium metal produced by the beam. Further oxidation after this provision is exhausted can only proceed by adsorbing oxygen from the residual gas or diffusion from deeper layers of the bulk. These processes are slow compared to the metal production rate, hence the curve in Fig. 5.34 exhibits a less steep increase.

The amount of oxygen that is dissolved in the lattice of the air cleaved crystals can be estimated from the metal production rate that was reported in [Bou97] ($1.15 \pm 0.1*10^{-9}$ cm^3/mC under irradiation at 190 K). An approximate correction factor of 3 for irradiation at 400 K as performed in this work instead of 190 K as accomplished by Bouchaala can be obtained from the same work. The volume of metal per surface area that is present in the crystal after irradiation with 100 mC/cm^2 at 400 K is thus about 4.5 10^{-7} cm^3/cm^2. This corresponds to 10^{16} calcium atoms/cm^2 distributed within the penetration depth of 2.5 keV electrons (70 nm, or 223 triple layers, see Fig. 2.13). By comparing this result with the number of CaF_2 molecules in the same layer, an average concentration of metallic calcium of 6 % after irradiation with 100 mC/cm^2 is obtained. For the purpose of this rough estimate, the same concentration within the probe depth of UPS is assumed. Provided each Ca atom reacts with one oxygen atom, a concentration of atomar oxygen of 6 % of the CaF_2 molecules is obtained.

This result is further supported by a direct comparison of the photoemission intensities of F2p and O2p peaks, neglecting differences in photoionization cross sections, which are assumed to be small for the two closed shell 2p ions. After irradiation with an electron dose of 108 mC/cm^2, the relative intensity of F2p and O2p emission was 6.5 %. This value corresponds to a concentration of 13 % oxygen within the sampling depth of UPS, since calcium ions are bound to two fluorine ions, but only one oxygen ion.

The oxygen related bandgap feature that was observed after irradiation of air cleaved crystals can be induced on UHV cleaved crystals as well by dosage of oxygen after electron irradiation. The UHV cleaved crystal used in this experiment was the same as the one from which the curves in Fig. 5.31 were obtained. After irradiation, the metallized surface was exposed to 15 L oxygen at a temperature of 550 K. A spectrum taken after oxidation is shown in Fig. 5.35 along with a spectrum from an air cleaved electron irradiated crystal not dosed with oxygen.

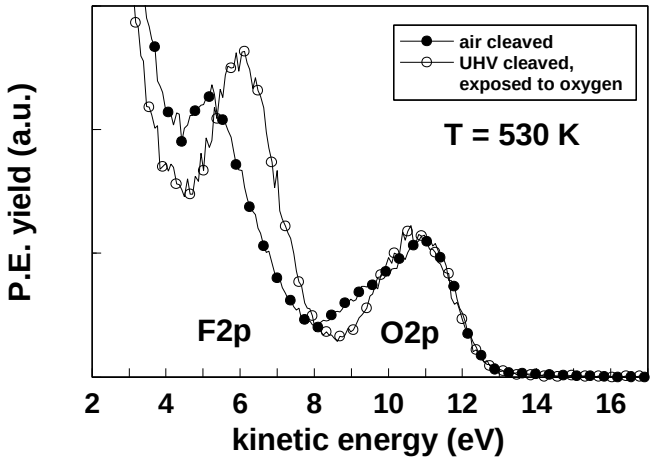

Fig. 5. 35 Ultraviolet photoelectron spectra of CaF_2(111) cleaved in UHV and in air after irradiation. The UHV cleaved sample was exposed to 15 L oxygen at a pressure of 5×10^{-8} mbar. The offset between the valence band peak positions is likely caused by the stronger background in the spectrum from the crystal cleaved in air. Oxygen features were shifted to the same position.

The spectra of the irradiated and oxygen dosed UHV cleaved crystal and of the air cleaved crystal measured after electron irradiation look very similar, which is another hint that the irradiation induced bandgap feature of air cleaved crystals is mainly caused by oxygen. This result also confirms that the oxygen peak observed on air cleaved crystals cannot be explained by assuming oxidation of calcium metal from the residual gas. The effect must be due to oxygen that is stored in the lattice of the air cleaved crystal, since the experiment performed with the UHV cleaved crystal, where no such structure was observed without oxygen dosage, was done under the same experimental conditions, in particular the same background pressure.

5.4.3 Electron irradiation effects at low temperature

The UPS investigations presented in this section originally aimed at the observation of electron beam induced *F*-center states similar to those presented in Fig. 5.22. It was shown by optical absorption spectroscopy of electron irradiated CaF_2 crystals that these defects immediately

aggregate to form Ca-colloids when irradiation was performed at 190 K [Bou97], however, at a lower irradiation temperature of 155 K, it was possible to observe the *F*-center absorption peak (see chapter 6). Thus, to suppress diffusion and to avoid the formation of metallic calcium states that cannot be detected by UPS with HeI excitation, experiments were performed on thin films at low temperatures of about 145 K.

Fig 5.36 shows a spectrum from a 12 nm epitaxial film before electron irradiation and two spectra recorded after electron irradiation at 145 K with dosages of 1.4 mC/cm^2 and 3.6 mC/cm^2, respectively. As a rough estimate, the higher dosage is expected to cause desorption of about 50% of the surface fluorine ions (compare section 7.5 on fluorine desorption from thin films). Photoemission was performed at a sample temperature of 145 K.

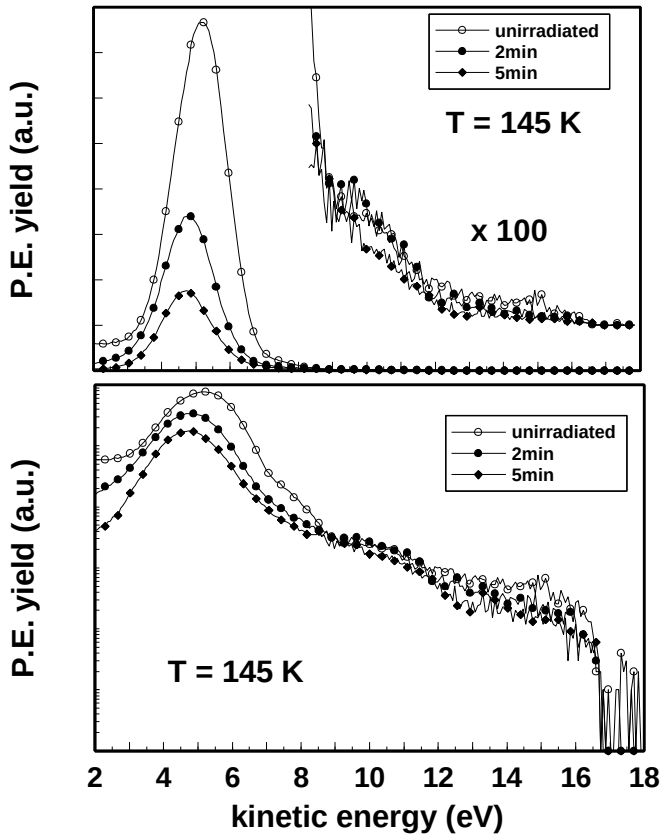

Fig. 5.36 Spectra taken from a 12 nm epitaxial film before and after irradiation at 145 K. Primary energy was 1.5 keV, Dosages of 1.4 mC/cm^2 (2 min irradiation time) and 3.6 mC/cm^2 (after 5 min irradiation time) were applied at a current density of 12 µA/cm^2.

No bandgap peaks like those in the spectra shown in Fig. 5.22 were observed after electron irradiation. Since irradiation with higher dosages did not improve the situation, it is concluded

that the lack of *F*-center emission is not due to insufficient concentration of this defect in the film, but to fast *F*-center aggregation into calcium aggregates in spite of the low temperature. Amorphous CaF_2 films were produced by evaporation of CaF_2 on SiO_2 at RT instead on Si(111) at a substrate temperature of 900 K. This was thought to disturb *F*-center aggregation into colloids, since the coherence between Ca^{2+} sublattice and metallic calcium lattice is destroyed. Fig 5.37 shows a spectrum from a 12 nm amorphous film before electron irradiation and two spectra recorded after 1.5 keV electron irradiation at 140 K with a dosage of 0.35 mC/cm^2 and 1.4 mC/cm^2, respectively.

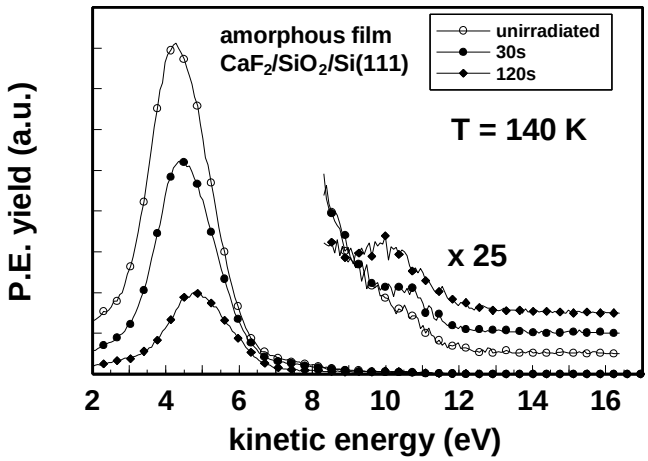

Fig. 5.37 Spectra taken from a 12 nm amorphous film that was evaporated on SiO_2/Si(111) before and after irradiation at 140 K. Primary energy was 1.5 keV at a current density of 12 $\mu A/cm^2$.

After irradiation, a small peak in the bandgap was observed that is attributed to beam induced reaction with oxygen from the SiO_2 substrate or from residual gas. However, also for this amorphous film, no *F*-center emission was observed.

5.4.4 Photon irradiation induced effects

UV irradiation with photons of 21.2 eV energy as was performed for photoelectron excitation also causes changes in the electronic structure of the material. Fig. 5.38 shows that under continued UV irradiation, a linear decrease of the F2p signal intensity was observed. The decrease in photoemission intensity is attributed to bulk defect creation by the incident UV light. Photoelectrons scatter at the defects, thus the mean free path is reduced. The effect is not due to a decrease in film thickness that may be caused by photon stimulated desorption. If this was the case, it should be possible to desorb a very thin film completely. However, this was not observed.

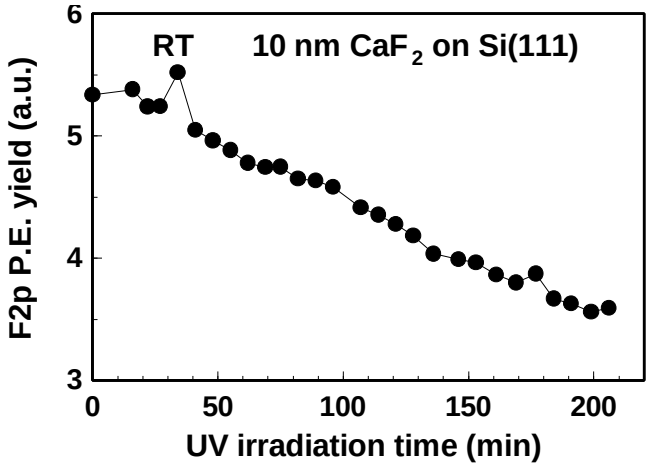

Fig. 5.38 Integral intensity of the F2p valence band peak taken from a 10 nm CaF_2 film. The intensity of the valence band peak decreases during HeI photon irradiation. This effect is not due to desorption, but to defect creation in the film. Photoexcited electrons are scattered at these defects, and the effective escape depths is reduced.

In Fig. 5.39, the first and the last spectrum from the measurement depicted in Fig. 5.38 are shown.

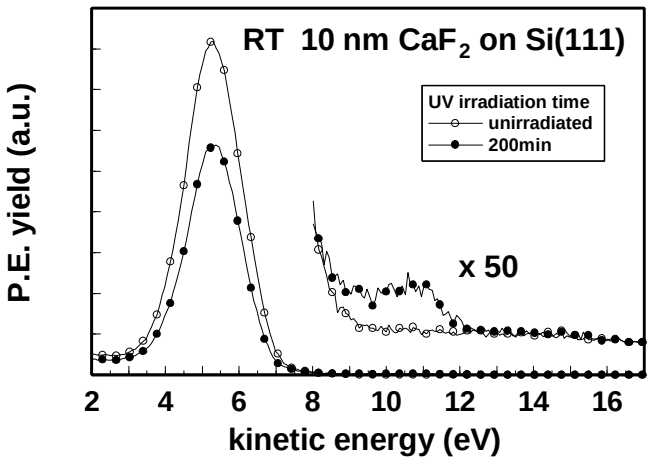

Fig. 5.39 Two spectra taken from a 10 nm epitaxial film immediately after starting exposure to 21.2 eV UV light and after 200 min of exposure to UV light, respectively. Apart from a decrease in valence band intensity, a small bandgap feature that is caused by irradiation induced oxidation from the residual gas is observed

Apart from the decrease in valence band intensity, only minor changes of the electronic structure were found. The small peak in the bandgap observed in the spectrum from the

irradiated film results from oxygen adsorption from the residual gas. Also after photon irradiation, no *F*-center states were observable.

5.4.5. Photon induced surface reactions with oxygen

In this section, oxygen adsorption during UV irradiation of crystals and thin films evaporated on Si(111) is investigated.

Fig. 5.40 shows the result of an oxygen dosage experiment with a UHV cleaved crystal under constant UV irradiation.

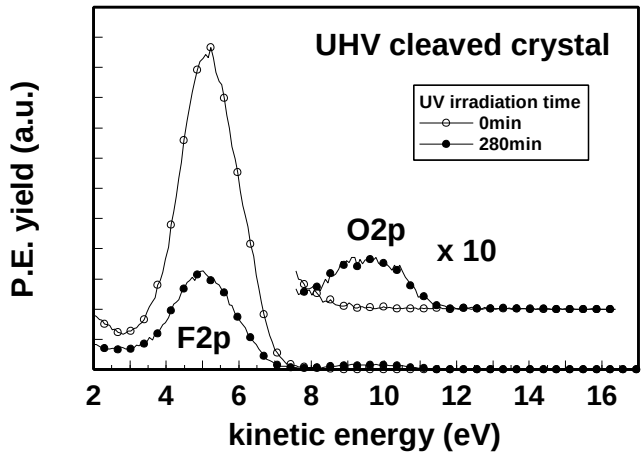

Fig. 5.40 Oxygen at a pressure of $5*10^{-8}$ mbar was dosed to an UHV cleaved sample at a temperature of 530 K. During the experiment, the sample was continuously irradiated with 21.2 eV photons. Simultaneous irradiation and oxygen dosage causes the formation of the O2p structure in the valence band of CaF_2. The energetic distance between the peak position of the F2p and O2p peak is 4.6 eV.

For crystals cleaved in UHV that are dosed with oxygen during UV irradiation, the formation of the oxygen related structure in the bandgap of CaF_2 is observed. A similar experiment was repeated with a crystal cleaved in air (Fig. 5.41) to see whether also a reaction of oxygen that is already dissolved in the lattice of a crystal can be induced by photon irradiation. It can be seen in Fig. 5.41 that no oxygen 2p structure was found after UV irradiation of air cleaved samples. From the different results obtained from both samples, it is concluded that the peak observed in the spectra measured from UHV cleaved samples is due to a reaction that takes place at the surface of the crystal. It is proposed that oxygen reacts with small metallic aggregates that are created during UV irradiation. Since oxygen arrives at the surface as a molecule, two calcium atoms are needed for a complete reaction:

$$O_2 + 4e^- \text{ (from calcium at the surface)} \rightarrow 2\ O^{2-}$$

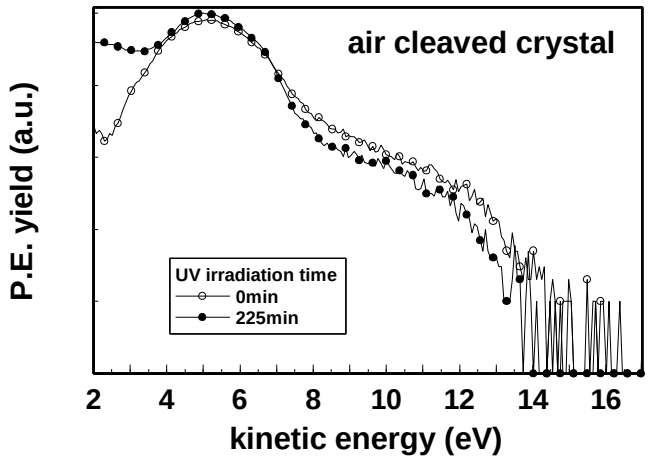

Fig. 5.41 Two spectra taken from an air cleaved crystal before and after 225 min of 21.2 eV photon irradiation. No oxygen 2p peak forms in the bandgap of air cleaved crystals during UV irradiation, in spite of oxygen is present in the crystal lattice as an impurity.

Oxygen adsorption was further investigated with thin films evaporated on Si(111). The dependence of the O2p yield on oxygen pressure and dosage time is shown in Fig. 5.42.

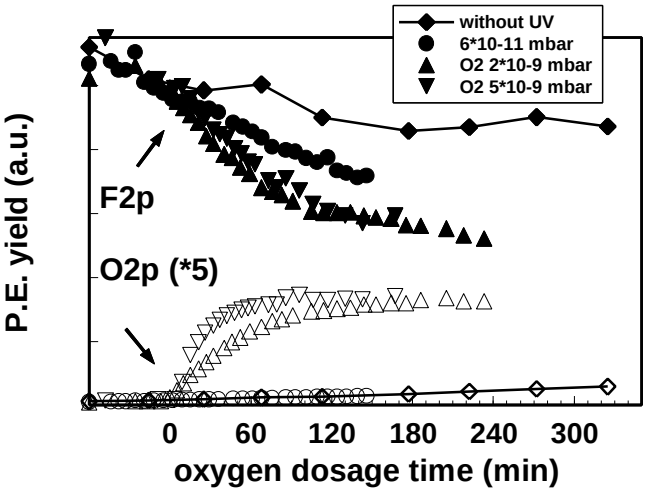

Fig. 5.42 General features in oxygen dosage of 10 nm CaF_2 films. The first two measurements were performed at a base pressure of $6*10^{-11}$ mbar without oxygen dosage. Without steady UV irradiation, only a slight decrease in F2p emission is observed. The O2p signal increases due to reaction with residual gas. Under constant UV irradiation, the F2p signal decreases more rapidly, but the increase in oxygen intensity is not higher than without UV irradiation. With oxygen dosage, the F2p peak decreases more rapidly than without, and the O2p peak emerges. All spectra were taken at RT.

It is concluded that the reaction to CaO was not limited by the irradiation intensity that determines the production rate of Ca metal, otherwise there should be no difference in the increase rate of the O2p peak with different oxygen pressures.

The diffusion range in thin films is limited by the substrate. Films of different thickness were prepared to compare their behavior during oxygen exposure (Fig 5.43).

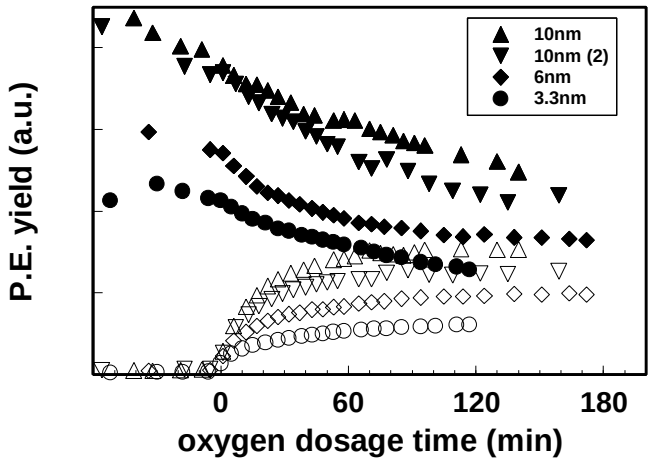

Fig. 5.43 Oxygen dosage of CaF_2 films of different film thickness. Oxygen pressure was $5*10^{-9}$ mbar. With decreasing film thickness, the F2p signal decreases as expected. The saturation value of the O2p signal also decreases with decreasing film thickness. This proves that oxygen is not limited to the surface, but diffuses into the bulk of CaF_2.

The O2p signal after saturation was found to be proportional to the film thickness. Oxygen is distributed uniformly through the film. Within the experimental error, the increase rate of the oxygen signal did not depend on film thickness. It is concluded that the velocity of oxygen diffusion is fast compared to the supply of oxygen from the surface.

By choosing appropriate preparation conditions, it was possible to produce amorphous films. By comparison of the results with those obtained from epitaxial films, the influence of the crystalline structure on oxygen diffusion in CaF_2 was determined. In Fig. 5.44, oxygen dosage to a crystalline and amorphous film is compared under identical experimental conditions. Oxygen does not penetrate into amorphous films as easily as into crystalline films. The effect may be due to grain boundaries or to a reduced number of interstitial sites in the amorphous film compared to crystalline samples. However, since the microscopic structure of these films is not well known so far, no definite assignment can be made.

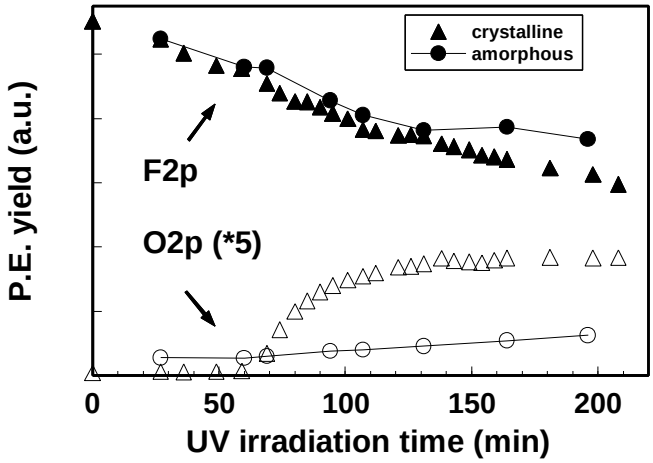

Fig. 5.44 Oxygen dosage of crystalline and amorphous CaF_2 films. Dosage was started at 60 min. Oxygen diffusion into the bulk of the amorphous CaF_2 film is hindered. Oxygen pressure was $5*10^{-9}$ mbar, the experiment was performed at RT.

5.4.6. Comparison of experimental results on oxidized CaF_2 surfaces to theoretical predictions

During his guest stay in our group, Vladimir Puchin calculated the electronic structure of the pure and oxygen covered CaF_2 surfaces [HPR98], [PPH98]. The CaO crystal has the rock salt structure with a lattice constant 10% smaller than that of CaF_2, and Ca ions form a cubic face centered sublattice in both crystals. This allows epitaxial growth of thin CaO film of (111) orientation on top of CaF_2 (111). The structure of the interface has been proposed in [ATO90] where also results from X-ray photoelectron diffraction experiments indicating the existence of such an oxide film are shown. The CaO (111) surface has a dipole moment and is therefore unstable unless it is reconstructed or covered by some adsorbate layer.

The following stable surface geometries were studied. (1) A sandwich structure, where the CaO layer is enclosed between two CaF_2 layers. In this configuration, there are two equivalent CaO (111)/CaF_2 (111) interfaces in the slab, and the open CaO (111) surface is avoided. This structure aimed to simulate oxygen that is dissolved in the lattice. (2) A CaO (111) 2×2 reconstructed film on CaF_2 (111). The surface has a three fold symmetry and small facets of (100) orientation. A drawing of this structure is shown in Fig. 5.45. (3) A CaOH film on CaF_2 (111). In this case, the top layer of F^- ions is replaced by OH^- ions oriented normal to the surface.

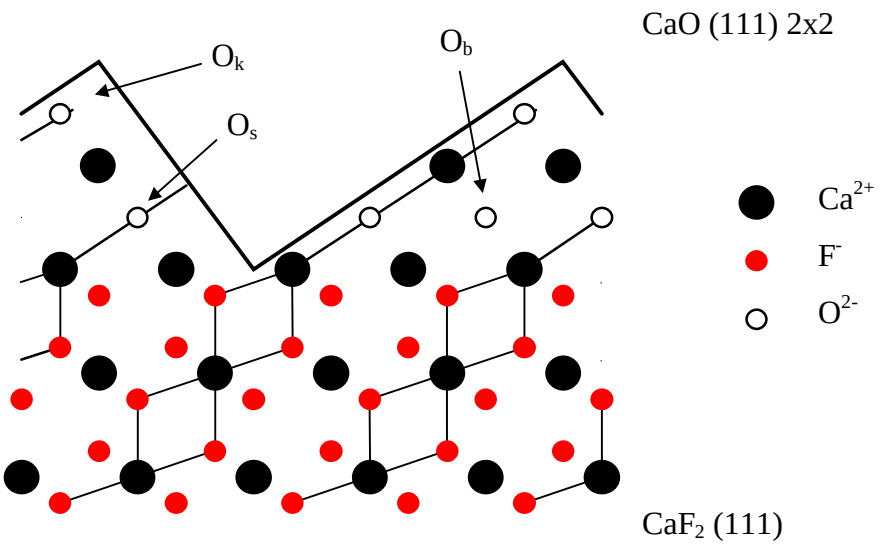

Fig 5.45 A three layer thick CaO (111) 2x2 reconstructed surface. The cross section shows two planes, the ions belonging to the first are connected by solid lines, while the ions belonging to the second plane are connected by dotted lines. The bold solid lines mark the actual surface that was calculated. The 2×2 reconstructed CaO surface contains three inequivalent O^{2-} ions with different numbers of nearest Ca neighbors, namely ions located in the bulk (6-coordinated, labeled O_b), at steps (5-coordinated, labeled O_s) and at kinks (3-coordinated, labeled O_k).

While optimizing the geometry for all slabs the lattice constant of CaF_2 was kept unchanged. Therefore, the CaO layers were stretched in lateral direction and consequently compressed in the direction perpendicular to the interface. The total density of states for all considered structures is shown in Fig. 5.46. Position and shape of the O2p band depend on the proposed atomic structure of the surface. In the case of the 2×2 reconstructed surface, there are three inequivalent O^{2-} ions with different numbers of nearest Ca neighbors. Therefore, the total density of states in the O2p band is a superposition of three bands corresponding to bulk (6-coordinated), surface (5-coordinated), and kink (3-coordinated) O^{2-} ions with peaks at 3.0, 4.4, and 5.8 eV above the top of the F2p band, respectively. A broad oxygen feature with a maximum at 4.0 eV was found for the sandwich structure. The OH^- peak in the density of states is at 1.6 eV above the F2p valence band maximum.

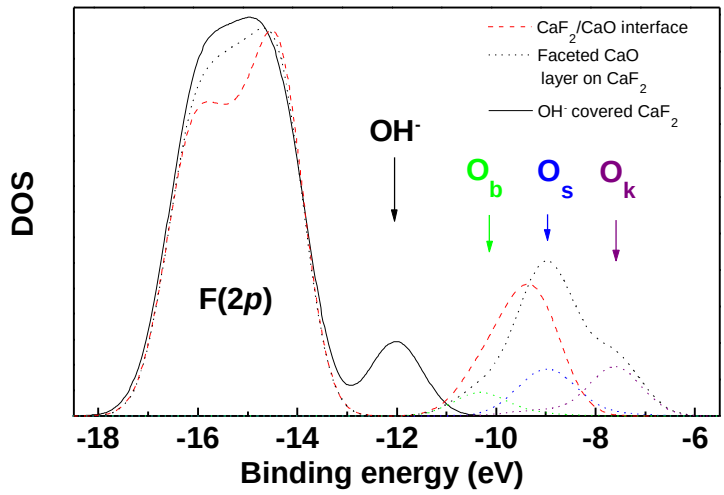

Fig 5.46 Calculated density of states (DOS) for the CaO/CaF_2 structures described in detail in the text. The sandwich structure gave a single peak at 4.0 eV above VBM (dashed line). The DOS of the reconstructed CaF_2/CaO surface is represented by the dotted lines. It consists of three contributions: states related to bulk (O_b), steps (O_s) and kinks (O_k) at 3.0, 4.4 and 5.8 eV above VBM, respectively. States from OH^- are found 1.6 eV above VBM (solid line). The absolute binding energies given in the figure are to some extend arbitrary and cannot be compared to the experiment.

Hence, photoemission results should reveal in which configuration oxygen is chemisorbed on CaF_2. For a comparison with experimental data, one has to correct for the different energy reference points used in both investigations. The calculated energetic distances between the

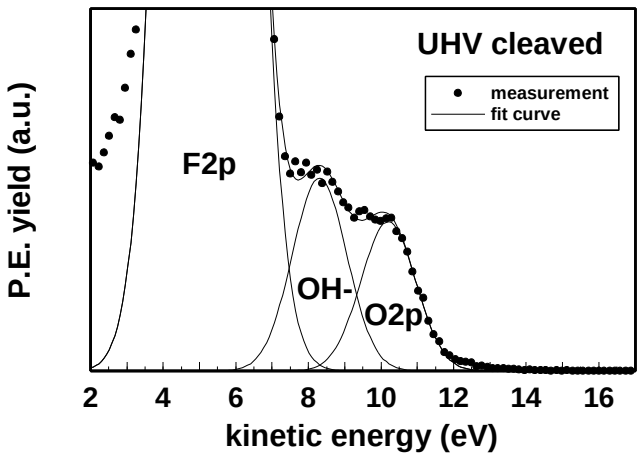

Fig. 5.47 Spectrum taken after oxygen dosage with simultaneous 21.2 eV photon irradiation of a CaF_2 crystal cleaved in UHV. Oxygen pressure was $5*10^{-8}$ mbar. Due to the high background pressure of $1*10^{-9}$ mbar during the experiment, also a reaction with water from residual gas occurred. Peak positions were determined by fitting three gaussian functions to the data. The positions are: F2p valence band: 5.24 eV, OH- peak: 8.3 eV, O2p peak: 10.2 eV.

peaks are given with respect to the F2p valence band maximum, while the experimental values are referred to the F2p valence band peak position. Thus, an offset of 1.6 eV accounting for half of the calculated valence band width in Fig. 5.46 is added to the calculated values. In Fig. 5.47, an experimental curve containing structures originating from adsorbed oxygen and OH- is shown.

The measured energy difference between F2p peak and OH^- peak is 3.06 eV compared to the calculated value of 3.2 eV. The experimental energetic difference between valence band peak and the oxygen structure is 4.96 eV. The calculation gives three alternative values for this distance, two of them corresponding to the bulk and step related oxygen peak of the 2x2 reconstructed structure which are at 4.6 and 5.0 eV above the valence band peak, and the value calculated for the sandwich structure, which predicts an energetic distance of 5.6 eV. Having in mind that, on the one hand, oxygen is dissolved in the lattice of CaF_2 as was shown above, and on the other hand, Hartree-Fock calculations tend to overestimate energetic distances, one would rather assign the measured oxygen feature to oxygen distributed in the CaF_2 lattice to which the sandwich structure is the closest description.

5.4.7 Summary

Effects of electron and photon irradiation on CaF_2 crystals cleaved in UHV and in air, and on thin films evaporated on Si(111) were investigated.

On both electron irradiated UHV and air cleaved crystals, a very strong reduction of the F2p valence band signal was observed, the magnitude of which was mainly attributed to a decrease in the photoelectron mean free path and only to a minor part to fluorine desorption. A similar decrease in valence band yield was observed during prolonged HeI photon irradiation.

No photoemission signal from calcium metal produced by electron irradiation on UHV cleaved crystals could be detected, due to the low cross section for the excitation of s-like calcium states with HeI radiation (21.2 eV).

On crystals that were cleaved in air, a reaction of oxygen dissolved in the CaF_2 lattice was observed under electron irradiation. From the saturation behavior of the oxygen structure, a concentration of oxygen in air cleaved crystal of about 6 % was estimated.

Photon induced reaction of CaF_2 with oxygen were observed when samples were exposed to oxygen during irradiation. No reaction took place when oxygen was already dissolved in the

lattice. When oxygen was dosed to thin films, it was found that the oxygen signal after saturation depended on the film thickness. It was concluded that oxygen is not limited to the surface, but penetrates into the bulk of the crystal or film. The results from crystalline films were compared to those from amorphous films. Here, oxygen did not diffuse into the bulk as easily.